Hazard Potential of Compound Flooding from Rainfall, Storm Surge, and Groundwater in Coastal New York and Connecticut

Robin Glas[1], Liv Herdman[1], Salme Cook[1], Archi Howlader[2], Kristina Masterson[1]

[1] U.S. Geological Survey, New York Water Science Center, Troy, NY, USA

[2] Akima Systems Engineering, Contractor to the U.S. Geological Survey, now at Kansas Geological Survey, Lawrence, KS, USA

Correspondence to: Robin Glas (rglas@usgs.gov)

Short Summary

We analyzed long-term groundwater, precipitation, and storm-surge records across coastal New York and Connecticut to estimate how often these hazards occur together. Overlap is highest along southwestern Long Island and western coastal Connecticut during the colder months, when groundwater is higher and mid-latitude cyclones are more common. Results from this study can support better preparation for coastal storms by taking into consideration the compounding effects of different flood drivers.

Abstract

Compound flood events, the co-occurrence of multiple flood drivers, can result in flood hazard potential exceeding that of any single driver alone. To evaluate compound flooding in a semi-urbanized coastal area, historical records dating back to 1970 are used to study the co-occurrences of high precipitation, storm surge, and shallow groundwater conditions along the coastlines of New York and Connecticut. Joint return periods for coincident precipitation-surge events were computed using statistical dependence models and compared to the assumption of independence as a ratio, referred to here as a return period adjustment. Results indicate distinct seasonality where compound events in the area disproportionately occur in the cold season between October and April. Return period adjustments range from a factor of 1 to almost 9, demonstrating the range in precipitation-storm surge dependence across the study area. Across all 24 station triad locations, groundwater levels were elevated during times of precipitation- surge co-occurrence, reflecting the tendency for coastal storms and shallow groundwater conditions to co-occur seasonally. The result is a pseudo-trivariate compound flood hazard score and corresponding hazard map that integrates dependence between daily precipitation-

surge events and overall monthly groundwater levels (as a precondition) into a relative compound hazard score. The location with the highest compound flood hazard score is on the south shore of Long Island, as well as locations across coastal Connecticut where groundwater levels compound the co-occurrence of heavy precipitation and storm surge.

1 Introduction

Coastal compound flooding, defined herein, is the concurrent or close succession of high precipitation and storm surge, and such flooding poses substantial challenges to communities along the East Coast of the United States (Nederhoff et al., 2024; Wahl et al., 2015). Coastal compound events have led to devastating impacts, resulting in loss of life (Hanchey et al., 2021), damage to property and infrastructure, and long-term economic effects (Green et al, 2024). Ghanbari et al. (2021) concluded that in recent years, the frequency and intensity of compound flooding have become more pronounced, exacerbated by climate change and sea level rise, highlighting the urgent need for refined risk assessments and mitigation strategies. Compound events, such as Tropical Storm Irene in 2011 and a historically important Nor'easter (colloquial regional meteorologic term for extra-tropical cyclones) in March 2010, caused wide-spread damage across the metropolitan area of the City of New York (hereafter "New York City"), with elevated storm tides and heavy precipitation occurring on top of soils that were already saturated or covered with antecedent snow (Orton et al., 2012).

This study focuses on compound coastal flood events and their geographic distribution around New York City, Long Island, and Long Island Sound, leveraging multiple historical records from precipitation stations, tidal gauges, and groundwater records spanning the past half-century. Previous studies have examined the occurrence of concurrent precipitation and surge events in this region utilizing tidal gauge data centred on a few stations near New York City, Montauk, N.Y., New London, Conn., and Bridgeport, Conn., for various data lengths and periods of record (e.g., Chen et al., 2024; Ghanbari et al., 2021; Nasr et al., 2023; Wahl et al., 2015). These studies indicate weak, positive dependences between storm surge levels and either precipitation or river discharge. The dependence of coastal storm surge between either precipitation depth or river discharge may be increasing in magnitude for hydrometeorological stations along the U.S. East Coast with teleconnections to climate

indices such as the Arctic Oscillation (Nasr et al., 2023). These previous studies have laid the groundwork for understanding the impacts of compound coastal events, and this study aims to enhance the existing body of knowledge by providing a higher spatial resolution analysis reviewing the geographic effects of proximity to the U.S. mainland and Long Island Sound on compound flood occurrence and groundwater conditions during these events.

Using copula models, the dependence between precipitation and storm surge for 24 precipitation-tidal station pairs are assessed across the study area. Copulas have been shown to be suitable statistical tools for understanding the relations between multi-dimensional random variables, particularly in the context of hydrological events (Salvadori and De Michele, 2007; 2010). Using a copula approach, the dependence between two or more continuous variables can be uniquely modelled independent of the marginal distributions, and multivariate nonexceedance probabilities can be computed for event pairs in more than one dimension (Favre et al., 2004). These nonexceedance probabilities can be expressed as bivariate return periods, most commonly for the OR case, where at least one variable exceeds a desired threshold, or for the AND case, where both variables are considered extreme (Brunner et al., 2016; Salvadori, 2004; Shiau, 2003). In this study, we consider the AND scenario when both precipitation and storm surge are simultaneously at their high concurrent levels.

Sea level rise, precipitation increases, and aging drainage infrastructure put shorelines at risk for more pronounced groundwater emergence, especially in coastal urban areas (Bosserelle et al., 2022). The coastlines of New York and Connecticut are discharge areas for the unconfined groundwater flow system characterized by shallow depths to groundwater and a high proportion of urban development (Rosenzweig et al., 2024). Groundwater flooding across heavily urbanized coastal areas will likely be exacerbated by sea level rise, in particular where the water table is no longer depressed because groundwater pumping has since ceased and where land filling practices have placed modern buildings and infrastructure over what used to be wetlands and drainage channels (Su et al., 2022; Bosserelle et al., 2022). Unconfined depth to water can be relatively shallow across coastal New York City, Long Island, and southern Connecticut (Bjerklie et al., 2012) (refer also to https://ny.water.usgs.gov/maps/li-dtw/ [accessed March 17, 2025]). We examine the occurrence of precipitation-storm surge compound events with shallow depths to water using historical groundwater data across the study area. The

interaction between these three factors can better inform the risk landscape for coastal communities during extreme weather events. Because monthly groundwater data preclude direct integration into the daily-scale return period framework, groundwater is treated as a preconditioning factor and incorporated through an ordinal scoring approach described in Section 3.5.

To illustrate the relative frequency of compound flood hazard across the New York City-Long Island-Long Island Sound region, comprehensive maps are presented that depict the spatial variations in the strength of dependence between precipitation and storm surge, along with the occurrence of shallow groundwater during these compound events. By describing the geographic distribution and interplay of flood drivers, this research furthers understanding of coastal compound flooding across coastal New York and Connecticut, to help inform stakeholders and decision makers about hydrologic hazards.

2 Study Area

This analysis focuses on the coastally influenced zone of Long Island Sound, comprising the southern Connecticut shoreline and lower tributary watersheds, the south shore of Long Island, and the coastal areas of New York City, bounded by the limit of direct tidal and coastal influence (Fig. 1). This boundary defines the geographic scope considered; however, observational coverage is not uniform across the full extent and results reflect the distribution of available monitoring stations. The region encompasses the densely populated coastal region along the northeastern United States, specifically focusing on Long Island (including the majority of New York City), and the northern shoreline of Long Island Sound, comprising the southern coast of Connecticut. People and property in this region have faced challenges from aging flood protection and drainage infrastructure (Coch, 2015; Forman, 2014), exposure to severe coastal flooding and erosion (Fallon and Kuonen, 2023), pronounced increasing trends in both extreme and annual precipitation (Kunkel et al., 2020), and sea level rise of approximately 10 cm over the past century that can be directly attributed to anthropogenic climate change and associated flood damages from tropical cyclones (Herreros-Cantis et al., 2020; Strauss et al., 2021).

Long Island, New York extends approximately 120 miles (193 km) eastward from New York City to Montauk Point and comprises four counties: Kings (Brooklyn), Queens, Nassau, and Suffolk.

With a population exceeding 7.8 million (U.S. Census Bureau, 2023), Long Island has development along much of the coastline. Groundwater dynamics of Long Island are influenced by its stratified aquifer system, primarily composed of sand and gravel that allows for efficient drainage and groundwater recharge (Walter et al., 2024). Areas where the depth to groundwater is shallow are vulnerable to flooding during heavy precipitation (Glas et al., 2023; Suffolk County, 2020).

Long Island has been impacted by devastating storms, with named storms including Tropical Storm Irene (2011) and Post-Tropical Cyclones Sandy (2012), and Ida (2021) having inflicted wide-spread damage across the region from heavy rainfall (localized flooding for areas lacking sufficient drainage), record breaking storm surges, and basement flooding (a basement being a floor or level of a structure that is below the ground level). Whereas these tropical storms have garnered substantial attention because their intensity and localized impacts, it is the more moderate extratropical cyclones that have been both more frequent and affect broader stretches of coastline, resulting in recurring flooding and storm surge events that affect a larger area (Booth et al., 2016; Liu et al., 2020). The combination of Long Island's exposure to cyclonic storm tracks and topography, low-lying coastal areas and marshes, along with intensive urban development make the region vulnerable to compound flooding, thereby drawing attention to water-management practices and coastal resilience planning (Rosenzweig et al., 2024). In particular, the southern shore is susceptible to flooding because of its shallow depth to groundwater, and exposure to storm tracks originating both from the U.S. mainland and the open Atlantic Ocean (Glas et al., 2023; Shepard et al., 2012).

Long Island Sound is a semi-enclosed tidal estuary located between Long Island, New York, and the southern coast of Connecticut, characterized by complex bathymetry and geography that substantially influence its susceptibility to coastal flooding (Liu et al., 2020). The relatively shallow depths of Long Island Sound (averaging about 60 feet, 18 m) allow for the amplification of storm surges (Kouhi et al., 2022; Wong, 1990), particularly during intense weather events, as observed during both tropical and extratropical storms (Booth et al., 2016; DeGaetano, 2008). Across the west-to-east gradient of Long Island Sound, storm generating mechanisms contribute to the severity of storm surge impacts, with extratropical cyclones causing the highest and most frequent surges in the western end of the sound, while

tropical storms and hurricanes create the largest surges in the eastern part near the open ocean (O'Donnell and O'Donnell, 2012).

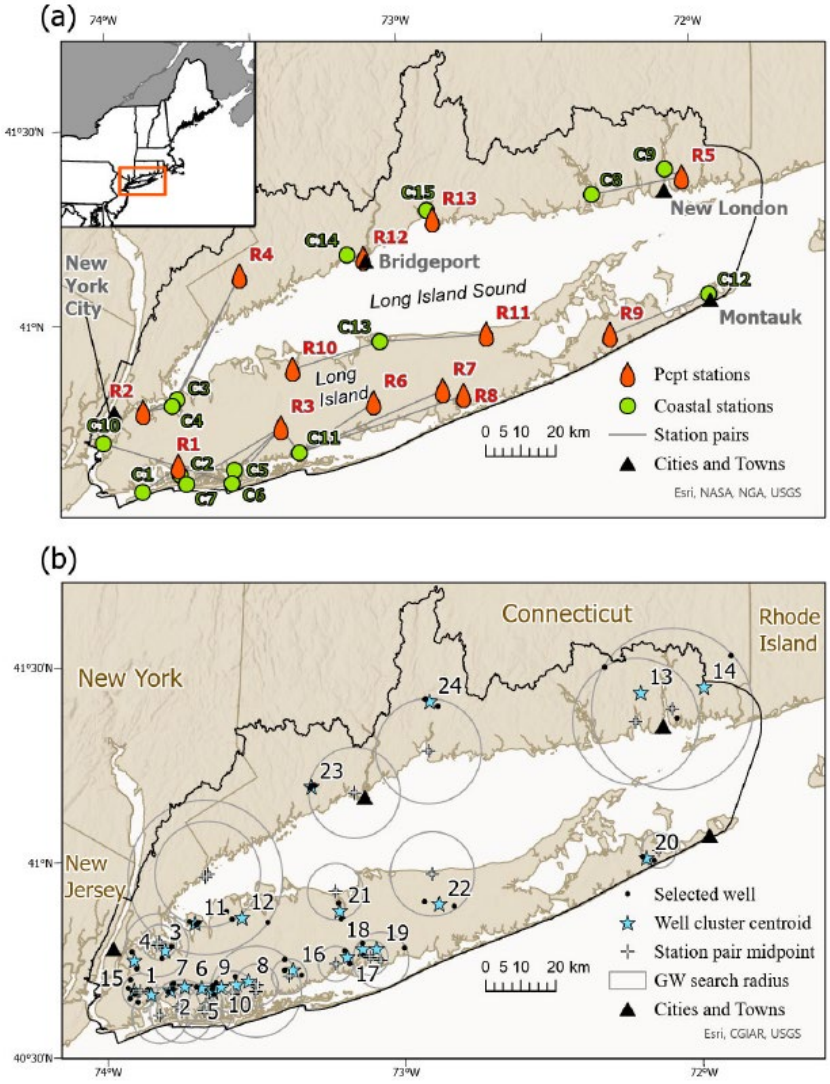

Figure 1. (a) Locations of precipitation, coastal water level, and groundwater observation stations used in the analysis; additional site information is provided in Table 1. Inset shows the location of the study area (orange box) within the northeastern United States. (b) Station triad locations, plotted at the nearest land point to the centroid of each triad composed of a precipitation gage, a coastal water level station, and a cluster of groundwater observation wells. Precipitation/surge midpoints are shown as the geographic midpoint between each precipitation and coastal station pair, with circular search radii indicating the area within which groundwater wells were selected for inclusion in each triad. The solid black line delineates the study area boundary in both panels. Projection World Geodetic System of 1984, Base modified from U.S. Geological Survey digital data, 1:1,250,000.

3 Data and Methods

3.1 Station selection and missing-record imputation

A total of 275 observing stations were considered for this study, located across the study area that includes the coasts or coastal regions of New York City, Long Island, and Long Island Sound (Fig. 1). Three data types were used in this analysis: (1) daily precipitation totals, (2) daily coastal non-tidal residuals representing storm surge, and (3) observed monthly groundwater levels measured in the uppermost unconfined hydrogeologic unit near the coast. First, total calendar day (24 hour) precipitation values were retrieved from 21 National Oceanic and Atmospheric Administration (NOAA) precipitation observing stations (NOAA NCEI, 2023) for a 52-year period spanning calendar years 1970 through 2021. On days when precipitation fell as snow, the liquid water equivalent was used as the precipitation value for that day as provided in the associated daily NOAA data report. Second, coastal water levels were retrieved from 12 NOAA water-level stations (NOAA CO-OPS, 2023) with recorded hourly water levels (meters) and 22 U.S. Geological Survey (USGS) water-level stations (U.S. Geological Survey, 2023) with recorded 15-minute water levels that have record lengths longer than 9.9 years between 1970 and 2021. A 33-hour low pass filter was applied to the observed hourly water level time series to compute the non-tidal residual (NTR), which is conceptually akin to "storm surge" (Cook and Herdman, 2025). The computed NTRs were subsampled to daily maximum values. Third, monthly groundwater levels were retrieved using the USGS National Water Information System (NWIS; U.S. Geological Survey, 2023) for 220 unconfined observation wells throughout Long Island, New York City, and southern Connecticut for the calendar years 1975 through 2021. A starting year of 1975 for groundwater optimized the record completeness based on data availability. Table 1 contains all station identification numbers, locations, and map I.D.s linking station locations to the maps in Fig. 1a.

Some real-time groundwater monitoring networks are available on Long Island at daily temporal resolution (U.S. Geological Survey, 2023) and can be used to analyse the response of groundwater to compound coastal flooding. However, the monitoring frequency is monthly for many wells with longer periods of record in Long Island, New York City, and Southern Connecticut. Therefore, monthly

175 groundwater observations were used in this study. The centroid locations of the groundwater wells selected for each station pair are shown in Fig. 1b; the well selection process is described in detail below.

Missing values for each of the three data types were filled using neighbouring, correlated stations at a daily timestep for precipitation and NTR, and at a monthly timestep for groundwater. The 180 imputations were carried out using the ARCHI R package (Levy et al., 2024, R Core Team, 2024, version 4.4.1), which iteratively searches the available input data for multiple correlated reference stations and uses regression to predict missing values at the target station. Each of the three data types were imputed using the ridge regression option within ARCHI, except for the case where only one reference station was available, and in that case simple linear regression was used. A Pearson 185 correlation coefficient of 0.6 and a Nash–Sutcliffe Efficiency (NSE) of 0.4 were used as the minimum threshold for accepted regression models in the ARCHI algorithm. Special consideration was given to the precipitation dataset because predictions from the ARCHI algorithm sometimes included near-zero negative values; predictions that were less than 1 mm were censored to zero. Full imputation statistics are shown in Supplemental Tables S1, S2, and S3 and the proportion of imputed to observed records 190 across the study area is summarized in Fig. 2. To further evaluate imputation quality, five percent of the observed values for each of the three data types were withheld (daily precipitation in millimeters, daily storm surge as NTR in meters, and monthly groundwater in feet below land surface), including separate consideration of wet day (observed prcp> 1 mm) and dry day (observed prcp < 1 mm) precipitation. The ARCHI algorithm then imputed those values and were compared to the observed values by root 195 mean squared error (RMSE) and bias. It should be noted that imputed records may retain missing values where no correlated reference station had concurrent observations available, for example, during early portions of the record when monitoring network density was lower.

Using the complete imputed data records, 24 precipitation-coastal station pairs were selected based on proximity. Each pair was subsequently paired with groundwater observation wells to form a 200 station triad, reflecting the three data streams contributing to each analysis location. Individual stations may contribute to more than one triad where geographic proximity warranted inclusion. Groundwater observation wells were selected using a cluster-based approach centered on the geographic midpoint

between each precipitation/coastal station pair in decimal degrees. Beginning with a 5-km search radius around each midpoint, wells were selected based on the following criteria: (1) at least 90% data availability from 1975 to 2021 in the imputed monthly time series, (2) 100% data availability from 2010 to 2021 to capture recent extremes, and (3) at least one observation of depth to water less than 50 feet (15 m) below land surface (bls), to exclude deeper aquifer zones or wells not representative of near-surface conditions. If fewer than two qualifying wells were found within the 5-km radius, the radius was incrementally expanded until the criteria were met. Final search radii for each midpoint are listed in Table 1, with a maximum of 23 km at Triad 12. Up to 10 wells per search radius were retained based on proximity to the precipitation-coastal station midpoint. Final selections were manually reviewed to confirm hydrogeologic consistency within each cluster, specifically that selected wells were completed in the same unconfined hydrogeologic unit, exhibited seasonal water level patterns consistent with neighboring wells, and were representative of ambient conditions. Final station triad groups are listed in Table 1 and respective group centroids shown in Fig. 1b. A list of all the selected wells and their associated triads are listed in Supplemental Table S4.

3.2 Precipitation-surge event sampling

To evaluate the relations between daily precipitation and storm surge, event pairs were selected and modeled using copulas with a "two-sided sampling approach" (Jane et al., 2022). Data were prepared for bivariate modeling by detrending coastal NTR (storm surge) values over a three-month moving window. No trends were detected in the daily precipitation time series. High or extreme events were identified in each dataset using a peaks-over-threshold (POT) approach, applying thresholds from the 90th to the 99th empirical quantile at each station. To ensure the selection of independent events, a declustering separation window of 10 days for precipitation and 6 days for NTR was established, which aligns with the lag times for considering concurrent events: ±5 days for precipitation and ±3 days for surge (Agel et al., 2015; Barbot et al., 2024). Final POT thresholds were chosen to limit the number of independent events per year to between 3 and 6 while maximizing the Kendall tau correlation coefficient between the two variables.

To create two distinct biconditional datasets the R package Multihazard (Jane et al., 2020) was used with the Multihazard::Con_Sampling_2D_Lag function. For the precipitation-conditioned dataset (CoP), 24-hour precipitation totals exceeding the selected threshold were identified as conditioning events, and the maximum NTR occurring within a ±5-day window of each precipitation event was extracted. For the surge-conditioned dataset (CoS), NTR values exceeding the selected threshold were identified as conditioning events, and the maximum precipitation occurring within a ±3-day window of each surge event was extracted. Time lags of ±5 days for CoP and ±3 days for CoS were based on findings that average coastal storm surge events around New York have durations ranging from 1.6 to 3.3 days (Barbot et al., 2024), and that the most common duration for extreme rain events in coastal areas of the Northeast is between 2 and 5 days (Agel et al., 2015). This approach accommodates potential mismatches between peak rainfall and storm surge that still have overlapping events, as well as delays in water reaching the coast via overland flow.

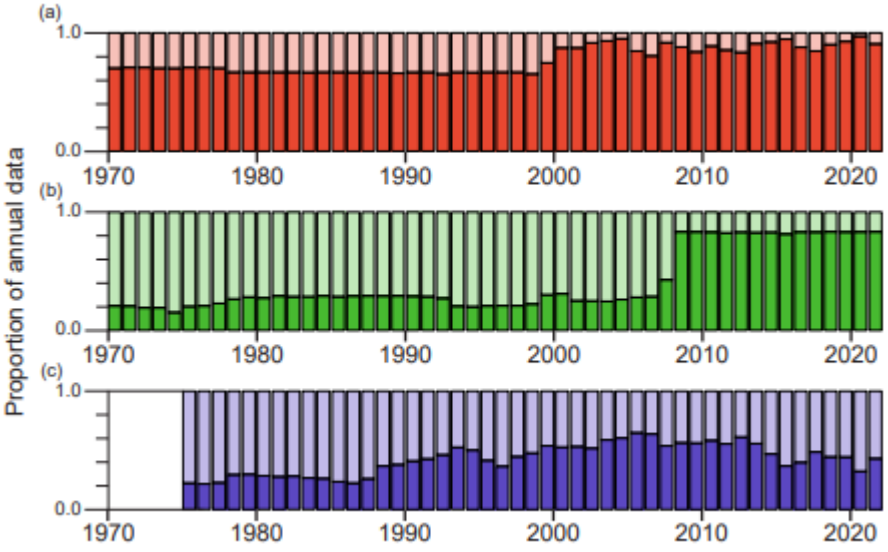

Figure 2. Proportion of observed (dark shading) and imputed (light shading) time steps for each calendar year. (a) Precipitation data (red; daily), (b) coastal non-tidal residual (NTR) data (green; daily), and (c) groundwater data (purple; monthly).

3.3 Precipitation-surge dependence

Biconditional precipitation-surge event sets were assessed for correlation using Kendall tau for each triad. Kendall tau is a rank-based nonparametric correlation coefficient that measures the strength of monotonic dependence between two variables, defined in Equation 1 as:

$$\hat{t} = \frac{n_c - n_d}{\frac{1}{2}n(n-1)} \quad (1)$$

where n_c and n_d are the numbers of concordant and discordant pairs respectively and n is the sample size. Kendall tau was used here because it does not assume normality of the marginal distributions, is robust to extreme values, and has a direct mathematical relationship to copula dependence structure through its connection to the copula parameter (Genest and Favre, 2007).

To identify temporal changes in this correlation structure, 20-year moving windows were used to re-compute the Kendall tau for selected events inside that time window, then shifted by one year across the time range of the dataset. To evaluate temporal changes in dependence structure, the empirical upper tail dependence coefficient ($\widehat{\lambda_U}$ hereafter referred to as uTDC) was computed separately for the first and second halves of the study period. The uTDC was estimated using Equation 2:

$$\widehat{\lambda_U} = \frac{1}{n_u}\sum_{i=1}^{n} I(U_i > u, V_i > u) \quad (2)$$

where U_i and V_i are pseudo-observations on the unit interval, I is the indicator function, and n_u is the number of observations exceeding the threshold u. Estimates were computed for u=0.6, representing the upper half of the distribution, and u=0.9, representing the upper tail. Calculations were performed for the periods 1975–1995 and 1996–2021 to assess changes in upper tail dependence over time and evaluate the need for a nonstationary framework. To further evaluate marginal stationarity, linear regression of POT exceedance magnitudes against time was performed for both precipitation and surge

across all 24 triads under both conditioning approaches. Slopes and associated p-values are provided in Supplemental Table S5.

To model the dependence structure in the data, each variable (precipitation and NTR) in the biconditional datasets was transformed into a uniform distribution by computing their rank-based pseudo-observations. The pseudo-observations are "plotting positions" using common nomenclature in hydrologic hazards (Asquith and others, 2017, app. 2), lie on [0,1], and correspond to the data mapped to rank-based cumulative probability space. An independence test of the pseudo-observation pairs was completed before selecting a copula model, where the null hypothesis is bivariate independence using the R function VineCopula::BiCopIndTest (Nagler et al., 2023, Genest and Favre, 2007). In the cases where the pseudo-observations are quantitively independent (p-value > 0.05), then the independence copula was selected for those station pairs. For bivariate data pairs exhibiting statistically significant dependence, parametric copula models were fitted using maximum likelihood estimation. The candidate set included two elliptical copulas: Gaussian and t, and three Archimedean copulas: survival Clayton, Gumbel, and Frank. These six copulas were selected to capture a range of tail dependence structures relevant to the variables of interest (rainfall and NTR). Specifically, survival Clayton and Gumbel exhibit upper tail dependence, the t copula exhibits symmetric tail dependence (both upper and lower), and the Gaussian and Frank copulas are tail-independent. These copulas are relatively common tools for practitioners and are all permutation symmetric, which means for the copula $C(u,v)$ that $C(v,u) = C(u,v)$. Such symmetry is therefore an implicit assumption for this study.

The best fitting copula was selected using the minimum Akaike information criterion (AIC, Akaike, 1973; Asquith and others, 2017, app. 4). The AIC offers a comparative measure of fit for candidate copulas, identifying the model with the lowest AIC as the optimal choice. In instances where the difference in AIC between the top candidate and the next best model was less than 2 ($\Delta AIC<2$), indicating a statistical tie in support, an additional screening was performed. Specifically, the empirical upper tail dependence coefficient (uTDC) of the observed data was compared against the distribution of uTDC values derived from 500 bootstrap simulations of each candidate model. If the absolute difference between the empirical uTDC and the median of the simulated uTDCs exceeded 0.1, the model was considered to provide a poor approximation of tail behavior and was excluded from

consideration. The remaining model with the better agreement in uTDC was selected. The uTDC threshold of 0.1 represents a meaningful departure given that empirical uTDC values across all 24 triads ranged from approximately 0.10 to 0.25 at u=0.6. The median rather than the mean of the bootstrapped uTDC values was used as the reference because bootstrap distributions of uTDC can be skewed under weak dependence or small sample sizes, making the median a more robust measure of central tendency. An absolute difference threshold was preferred over a standard deviation based criterion because uTDC is bounded on [0,1], making absolute comparisons on the same scale more interpretable.

Graphical diagnostics and a goodness-of-fit hypothesis test were used to assess absolute fit and ensure that the selected model adequately represents the raw data. The quality of fit was graphically inspected by comparing the fitted parametric copula to the empirical copula by contour lines along cumulative probability values (the "level curves" in copula nomenclature, not shown). Additionally, a rank-based goodness-of-fit test was applied to further assess the fit of the selected copulas (Huang and Prokhorov, 2014). This test is semi-parametric, using a parametric copula and nonparametric, empirical marginals where the null hypothesis pertains to the assumption of the data following the specified copula model using the VineCopula::BiCopGofTest function in the VineCopula R package (Nagler et al., 2023).

When computing return periods for bivariate data using copulas, there are an infinite number of data pairs (precipitation-surge) associated with a single joint return period that can be graphically represented by contour lines instead of univariate singular estimates. All joint return periods computed in this study are AND-type, corresponding to the simultaneous exceedance of both precipitation and surge thresholds, as distinct from OR-type return periods where exceedance of either variable alone is sufficient. Return period contour lines associated with each biconditional dataset were computed using the fitted copula through Eq. 2 for the AND joint return period, examining the probability of a specific magnitude of precipitation and coincident surge:

$$RP_{AND} = \frac{\mu}{1-u-v+C(u,v)} \quad (3)$$

where μ is the average interarrival time of events in years, and u and v are the marginal cumulative distribution functions (CDFs) associated with each variable, and C(u,v) is the joint CDF of the selected copula function. For a fixed return period T, Equation 3 is satisfied by a continuous set of (u,v) combinations lying on [0,1] x [0,1], defining a contour line in bivariate probability space rather than a single point estimate. Under the assumption of independence, the joint AND return period is the product of the two marginal return periods, incorporating their respective exceedance probabilities. In contrast, under dependence, this relation is altered, and for positively correlated variables, the joint AND return period is shorter than under the independence assumption.

For each triad, and for the subset of univariate marginal return periods of 2, 10, 25, 50, and 100 years for both precipitation and surge, the ratio of the bivariate AND return period under independence to the dependence case was calculated for each combination of univariate return periods using the selected copula model. This ratio of return periods, or return period adjustment, represents the degree of dependence between the variables across each unique combination of univariate return periods (u and v), allowing the measure of dependence between the variables to be assessed in units of return period (Zscheischler and Seneviratne, 2017). To illustrate, consider a precipitation event with a univariate return period of 4 years and a coincident surge event with a univariate return period of 50 years. Under the assumption of independence the joint AND return period is the product of the two marginal return periods: $4 \times 50 = 200$ years. Under dependence, if the return period adjustment factor is 8, the joint AND return period is $200 / 8 = 25$ years, meaning the compound event is 8 times more likely to occur than independence would predict.

3.4 Precipitation-surge compounding and uncertainty

To simplify the suite of return period adjustments across the unique u and v combinations, the array of return period adjustments was collapsed to a single value by weighted averaging. For each triad location, the paired events were randomly sampled 500 times with replacement, preserving pair structures and number of bivariate events. Copula parameters were re-estimated while maintaining the copula family type of the full dataset, and bivariate return periods and their corresponding adjustments

from the independence case were re-computed. From the resulting distribution of return period adjustments corresponding to each unique pair of univariate marginal return periods, the 0.025 and 0.975 quantiles were extracted and used as 95% confidence intervals around each return period adjustment. The width of the 95% confidence interval is representative of bivariate sampling uncertainty around the return period adjustment calculations, and the inverses of these widths were used as weights in the final weighted averages of return period adjustments for the CoP and CoS paired values for each station triad. This results in two weighted average return period adjustments per station triad. The weight assigned to each return period adjustment was computed according to Equation 4:

$$w_i = \frac{1}{CI_i} \quad (4)$$

Where CI_i is the width of the 95% confidence interval for the return period adjustment at univariate return period combination i, derived from the 500 bootstrap samples. The weighted average return period adjustment for each triad was then computed according to Equation 5:

$$\overline{RP} = \frac{\Sigma_i w_i \cdot RP_i}{\Sigma_i w_i} \quad (5)$$

Where RPi is the return period adjustment at each unique combination of univariate marginal return periods. This weighting scheme assigns greater weight to return period combinations where bootstrap uncertainty is smallest, which in practice corresponds to shorter univariate return periods where sample sizes are largest. The resulting return period adjustments and bootstrap uncertainty for each triad are presented in Section 4.4.

3.5 Groundwater and composite score

For each triad, median monthly groundwater levels were computed from the selected wells within each associated cluster. These monthly time series were linearly interpolated to daily resolution. Groundwater levels (in feet bls) were then extracted for the date of each event type: rainfall above threshold, surge above threshold, and concurrent rainfall/surge events. This extraction enabled assessment

of groundwater conditions during different types of compound events. Because the groundwater levels may not have been measured during the actual storm event, the values used in this analysis may not represent the actual groundwater response to coastal and precipitation events.

To characterize groundwater-related hazard, the shallowest groundwater levels (minimum depth to water bls) during any compound event (both CoP and CoS) were used to assign a groundwater hazard score. Depths of 6 ft (1.8 m) or less were assigned a score of 2 (high hazard), depths between 6 ft and 15 ft (1.8 to 4.6 m) were scored as 1 (moderate hazard), and depths > 15 ft (4.6 m) were scored as 0 (low hazard). These thresholds reflect physical infrastructure vulnerability criteria: depths less than 6 ft have the potential to interfere with drainage infrastructure and natural soil infiltration (Bosserelle et al., 2022), while depths between 6 and 15 ft are likely to intersect with basements and subsurface infrastructure (Conestoga-Rovers and Associates, 2007; New Jersey Department of Environmental Protection, 2021). These thresholds are consistent with those used in the companion groundwater emergence hazard analysis for the same study area (Masterson et al., 2025; Welk et al., 2025a), for direct comparison of hazard scores across the suite of regional hazard products.

The groundwater hazard score was combined with two scores based on the dependence structure between precipitation and surge. First, a triad received 1 point if either CoP or CoS event datasets exhibited upper tail dependence, as determined by fitting a copula with upper tail dependence. Second, a triad received 1 point if symmetrical dependence was observed, meaning a non-independent copula was selected for both CoP and CoS event types.

The three component scores (groundwater depth, upper tail dependence, and dependence symmetry) were summed and rescaled to yield a final compound hazard score ranging from 1 (lowest) to 5 (highest) for each triad.

To interpolate these results across the entire study area (the coasts of Long Island Sound and the south shore of Long Island), each groundwater centroid location was initially assigned to one of eight clusters using *k*-means clustering (MacQueen, 1967), implemented with the scikit-learn Python library (Pedregosa et al., 2011). Clustering was based on the following six features: (1) average return period shift conditioned on precipitation (CoP), (2) average return period shift conditioned on surge (CoS), (3) median minimum groundwater depth (in feet), (4) groundwater hazard score, (5) biconditional

dependence score, and (6) upper tail dependence score. The number of clusters (k) was selected by evaluating silhouette scores over a range of candidate k values; the highest score occurred for k=8. Because k-means does not enforce geographic contiguity and some of the statistically derived clusters consisted of multiple disconnected spatial regions, a spatial post-processing step was applied to separate Connecticut and the North and South shore of Long Island. Non-contiguous cluster components were separated into distinct regions to ensure that each final cluster represented a coherent geographic unit. This procedure resulted in 9 final regions, each containing between one and four stations, while preserving the underlying k-means classification structure.

For each cluster, a centroid was calculated and used to generate Voronoi polygons (Aurenhammer, 1991) that partitioned the entire study area. Separate Voronoi tessellations were created for Connecticut (CT), and for the north and south shores of Long Island. Within each Voronoi polygon, 900-meter grid cells were assigned the average compound hazard score of the stations in the corresponding cluster. Averaging was then masked and restricted to 900-meter grid cells located within the coastal 100-year flood (0.01 annual exceedance probability) hazard extent for the study area, as defined by Welk et al. (2025b). This grid is the same grid used for rainfall hazard (Welk et al., 2025b), coastal flood hazard (Cook and Herdman, 2025), and groundwater hazard (Welk et al., 2025a) across the same study area, allowing for direct spatial comparison of hazard scores across variables. The spatially continuous hazard map is based on interpolation of results from discrete monitoring stations. These stations are assumed to be representative of broader conditions, but the map does not account for local variability in precipitation,

coastal water levels, or groundwater depth at locations where no measurements were available. The analytical workflow for compound flood hazard assessment, from data imputation through spatial interpolation of hazard scores, is summarized in Fig. 3.

420

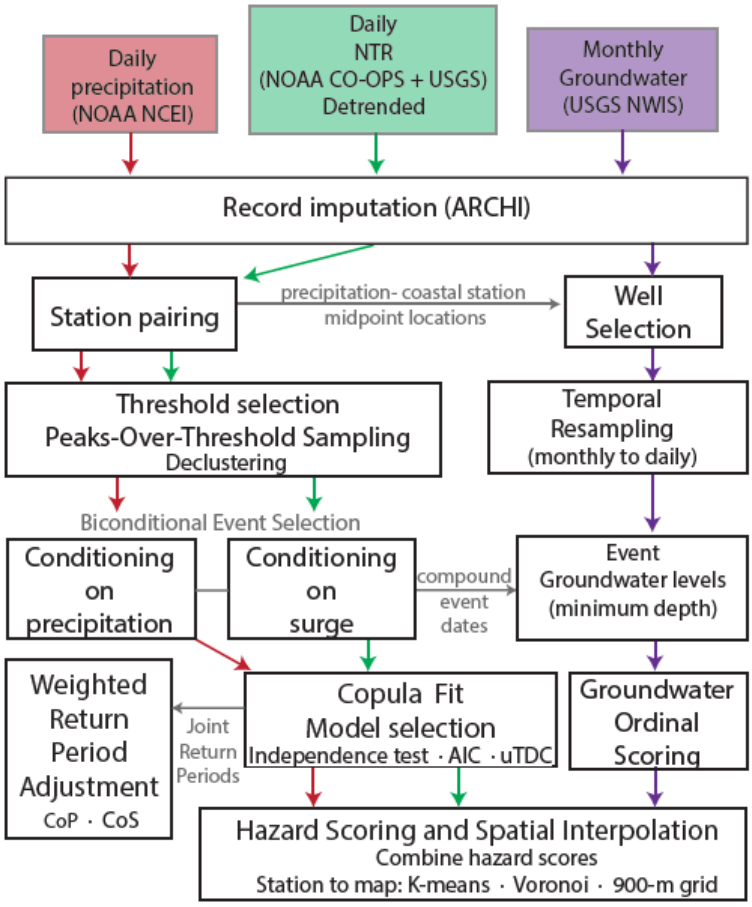

Figure 3. Flowchart summarizing the analytical workflow for compound flood hazard assessment. Three data streams -- daily precipitation (red), daily non-tidal residual storm surge (green), and monthly groundwater (purple) -- are processed through station triad design and imputation, biconditional event sampling, copula fitting and model selection, and return period adjustment. Groundwater is incorporated as a preconditioning factor through a separate scoring step before all components are combined into a final compound hazard score and interpolated across the study area. CoP, conditioned on precipitation; CoS, conditioned on surge; AIC, Akaike information criterion; uTDC, upper tail dependence coefficient; ARCHI, Automated Regional Correlation Analysis for Hydrologic Record Imputation (Levy and others, 2024).

4 Results

4.1 Imputation quality

A total of 21, 34, and 207 observing stations were used to fill in missing records for precipitation, coastal NTR, and groundwater, respectively. Then, a subset of these stations, 13 precipitation, 15 coastal, and 58 groundwater observing stations, were used after imputation for input to the copula models and the final combined compound flood hazard score. The proportions of observed and imputed values are presented in Fig. 2 for these stations, separated by each year of record from 1970 through 2021. Precipitation data had more than 80% observed values throughout the study period, whereas observed values for coastal NTR averaged about 15% until 2008 and 80% through 2021. Observed data comprised about 20% of groundwater records for 1975–1990, after which the proportion of observed records increased to between 40% to 60%. Despite the high proportion of imputed values in the NTR and groundwater datasets, their strong intrinsic correlation and sufficient duration of overlap justified their inclusion. Precipitation data exhibited lower cross-correlation; however, at least 80% of precipitation values were observed in any given year of the study period, exceeding the proportion of observed values in the NTR and groundwater datasets. Errors (RMSE and bias) were higher than for coastal water levels or groundwater, reflecting the greater spatial and temporal variability of precipitation (Supplemental Tables S1 – S3). However, because the precipitation record contained a high proportion of observed values, only a small fraction of the series was imputed, limiting the influence of these higher errors.

The accuracy of the regression imputation process was assessed using the results from the holdout analysis, comparing observed to imputed across precipitation, coastal NTR, and groundwater datasets (Table 2). Higher error and bias resulted from wet-day precipitation values, where imputation on wet days were on average 1.5 mm lower than observed values, and dry-day imputations were on average 0.34 mm higher than observed (zero) values (Table 2). Taken as a whole, holdouts from the entire precipitation dataset were on average 0.08 mm lower than observed values. Corresponding RMSEs for each precipitation holdout dataset were highest for wet days, lowest for dry days, and approximately 4.5 mm for all precipitation days as a whole. The NTR and groundwater datasets were

slightly under-predicted by the imputations; however, these errors were relatively small (less than 1/100 of a meter and foot, respectively). Full imputation statistics for the entire dataset (not withheld values) are provided in Supplemental Tables S1–S3.

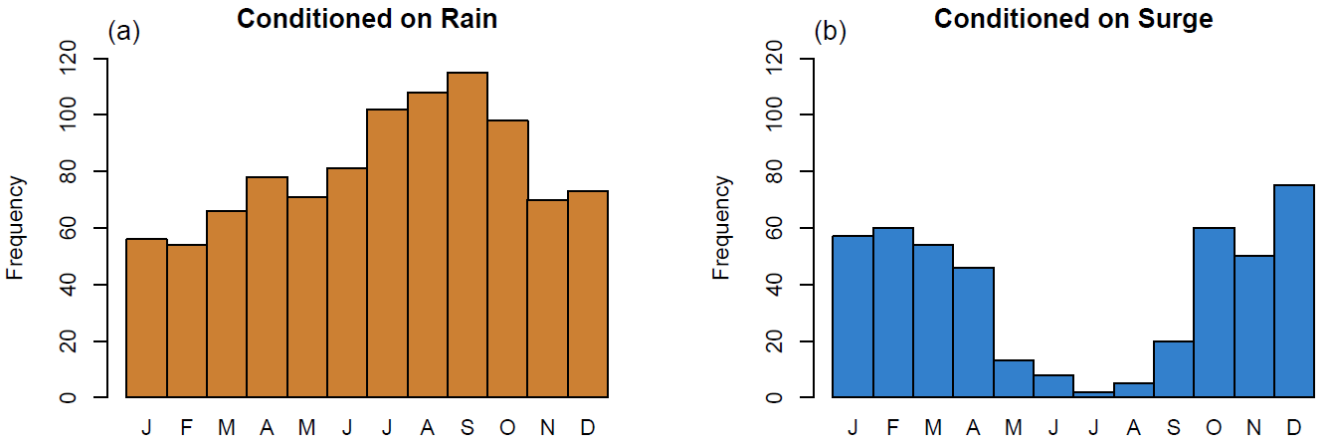

Figure 4. Monthly seasonality of unique concurrent events exceeding defined threshold quantiles, pooled across Triads 1 through 24. Events include rainfall/surge pairs selected from either (a) precipitation-conditioned (CoP) or (b) surge-conditioned (CoS) samples. Months are labeled on the x-axis by their first letter.

4.2 Biconditional sampling

Selected precipitation and surge threshold probabilities ranged from 0.97 to 0.99 across precipitation and surge datasets for all 24 triads (Table 3) and resulted in the average number events ranging from 3.1 to 5.8 events per year. Selected events conditioned on precipitation (CoP) showed a slightly seasonal pattern during the warmer months of the year, whereas events conditioned on surge (CoS) occurred distinctly between the months of October to April (Fig. 4). Sample size also varied across triads and sampling conditions, ranging from 162 (triad 23, CoP) to 308 precipitation-surge events (triad 22, CoP). Correlations across both datasets were weak, with higher and more substantial correlations when data were conditioned on surge. Mean Kendall tau of conditional datasets were 0.06

for CoP samples, and 0.13 for CoS samples. An example of data for triad 15 (The Battery, NY) with selected precipitation and NTR thresholds is shown in Fig. 5.

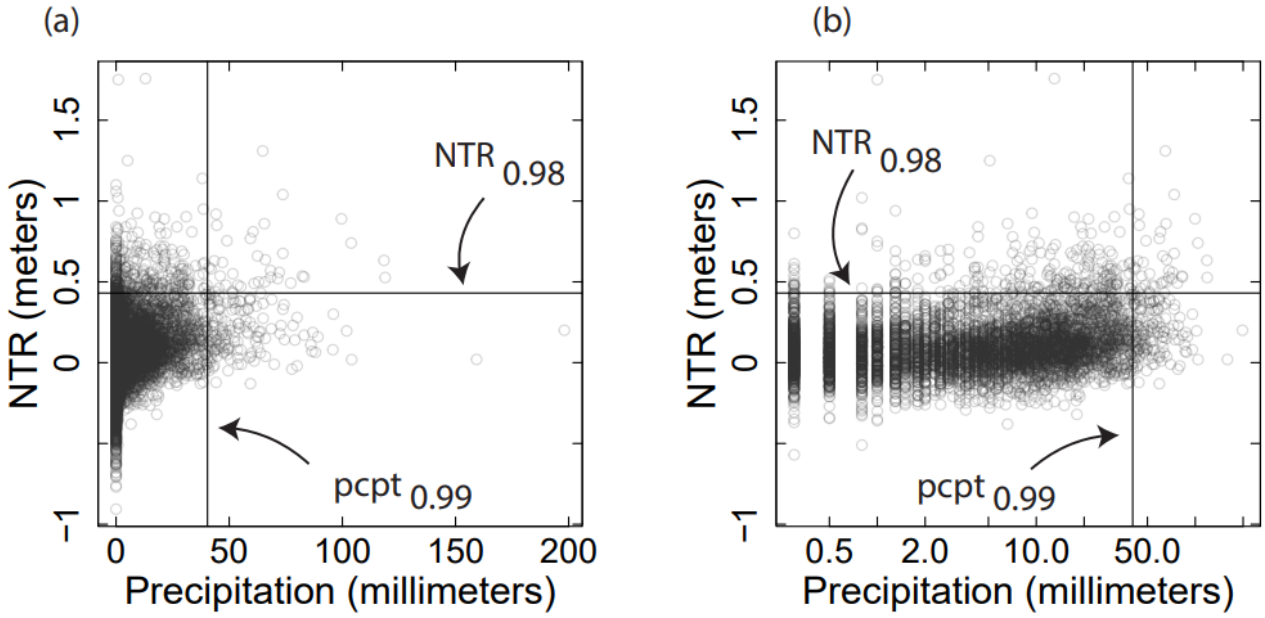

Figure 5. Daily precipitation and non-tidal residual (NTR) data for Triad 15 (Battery, NY), including selected fractional percentile thresholds for each variable. (a) Data shown in real space; (b) data shown on log-transformed axes with zero values excluded.

4.3 Dependence

Sampled events that were conditioned on surge showed more dependence than those conditioned on precipitation based on selected copula models. Of the triads exhibiting statistically significant dependence, upper tail dependence was present in 6 of 24 triads under CoP and 12 of 24 triads under CoS, as determined by selection of a copula family exhibiting upper tail dependence (Table 4). Independence was evident in 14 of the 24 triads where event selection was conditioned on precipitation, whereas only one of the triads (triad 10) was found to have independent data when events were conditioned on surge. For events conditioned on surge, 12 of 24 triads exhibited upper tail dependence

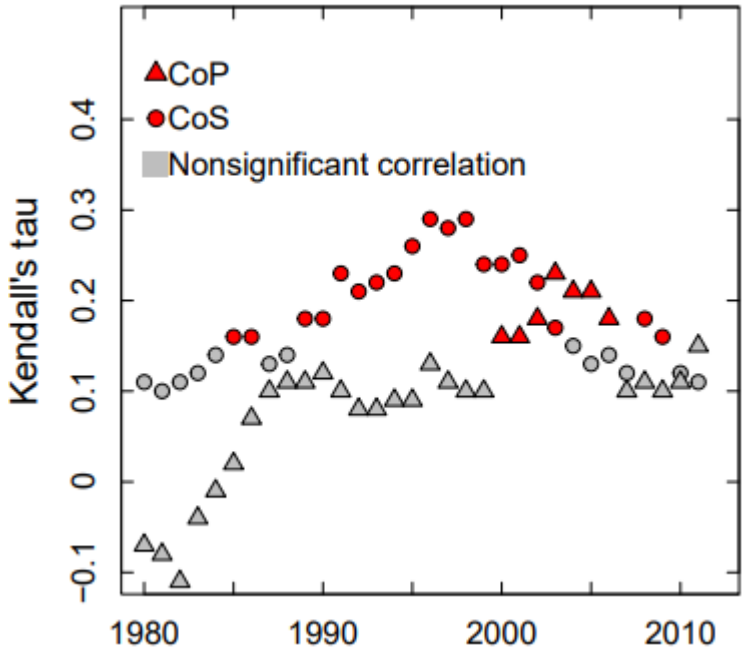

Figure 6. Time-varying Kendall correlations for triad 15 (refer to Figure 1 for location), computed using a 20-year moving window shifted by one year. Correlations are based on selected precipitation/surge events under both sampling conditions: conditioned on precipitation (CoP) and conditioned on surge (CoS). Statistically significant correlations ($p < 0.05$) are shown in red.

(Table 4). Changes in Kendall tau for the period of study (1970–2021) were either slightly positive or slightly negative across all 24 triads but increased on average less than 0.1 over the study period (e.g.,

Triad 15, Fig. 6). Changes in the nonparametric upper tail dependence coefficient during the first half (1970–1995) to the second half (1996–2021) of the period evaluated in this study showed no persistently increasing or decreasing patterns across the 24 triads (Fig. 7). Regression of POT exceedance magnitudes against time revealed no regionally coherent trend in precipitation extremes across the 24 triads. Surge extremes showed slight decreasing trends at a subset of triads along the western south shore of Long Island and coastal Connecticut, with slopes ranging from -0.003 to -0.007 m/year (Supplemental Table S5). The direction of these trends is conservative with respect to compound hazard assessment. Based on these results, stationarity was assumed for this analysis.

For samples for which independence could not be ruled out, the independence copula was assigned; this explicit "snap" to independence means that reliance on a given nonindependent copula model with its empirical parameter was not made for this study (Table 4). Graphical comparison to the empirical copula (not shown), and p-values from the semi-parametric goodness-of-fit (GOF) test indicate the copula chosen by the AIC and uTDC criteria acceptably fit with the empirical data (p-values for GOF test shown in Table 4). Model fit diagnostics for all candidate models are shown in Supplemental Tables S6 and S7.

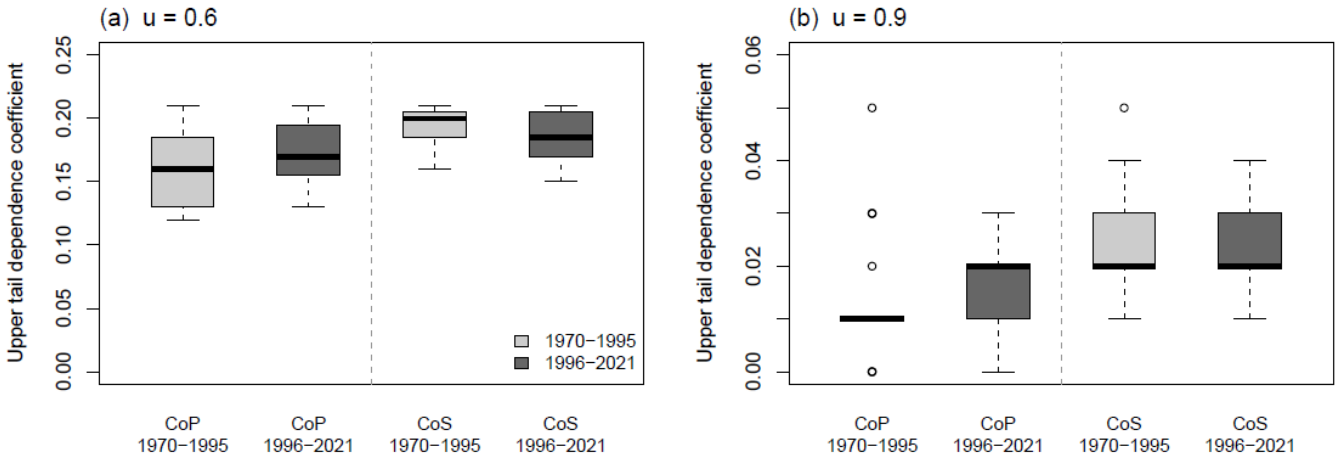

Figure 7. Empirical upper tail dependence coefficients (uTDC) for the first (1970-1995, light grey) and second (1996-2021, dark grey) halves of the record, shown for (a) u=0.6 and (b) u=0.9. Distributions are shown separately for precipitation-conditioned (CoP) and surge-conditioned (CoS) samples across all 24 triads. Overlapping distributions and similar medians between periods support the assumption of stationarity in the dependence structure.

4.4 Precipitation- surge return period shifts

Figure 7 and Table 5 show and list, respectively, the results from the copula analysis as return period adjustments between the assumption of independence and dependence for concurrent precipitation-surge events. The weighted average return period adjustment encompasses all values across the selected univariate return period pairs, inversely weighted by the variability from the bootstrap resampling (Fig. 8a). Because higher return period adjustments generally indicate more variability between the bootstrapped samples, the weights put more emphasis on shorter univariate return period events. Fig. 8b illustrates this for Triad 15, showing how the return period adjustment varies across univariate return period combinations for surge along with associated 95% confidence intervals. The curvature of this relationship reflects the two-dimensional nature of the joint AND return period contour described in Equation 2, where each point along the curve represents a different (u,v) combination satisfying the same joint exceedance probability. Weighted average adjustments ranged from 1 (independent data) to 8.51 (Triad 4, conditioned on surge, Table 5), meaning that coincident rain-surge events are more than eight times more likely to occur when taking their dependence structure into account (that is, the joint AND return period under dependence is approximately eight times shorter than under the assumption of independence, reflecting the observed historical dependence structure rather than any change in physical forcing). The average return period adjustment conditioned on precipitation was 2.99, whereas the average adjustment conditioned on surge was 4.32 across all station triads. The magnitude of period adjustments corresponds to the strength of upper tail dependence associated with the copula models as well as statistically significant correlations represented in the Kendall tau correlation coefficient (Tables 3 and 4).

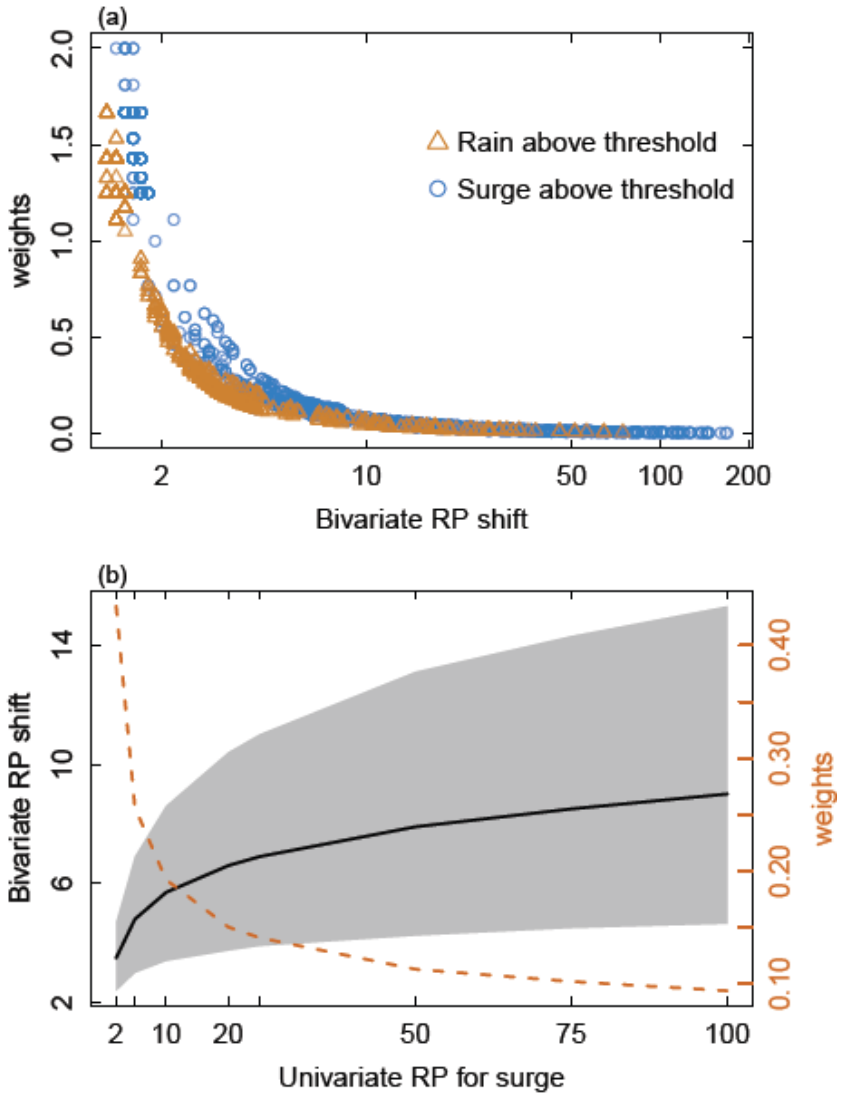

Figure 8. Precipitation–surge return period (RP) shifts versus weights used in the final averaging. (a) All triads combined. (b) Example of 95% confidence intervals (shaded area) for return period shifts corresponding to the 50-year univariate return period for rainfall, shown for triad 15 at Battery, NY. Weights across univariate return periods shown in orange dashed line.

4.5 Groundwater and Multivariate rating score

Over the 1975–2021 period of data, the shallowest (minimum) depth to groundwater during pooled compound event dates was extracted for each station triad's well cluster and used to assign the groundwater hazard score (Table 5). Groundwater shallower than 6 feet or 1.8 m was associated with triads 17 and 23 along the southern shore of Long Island and Connecticut, respectively. Depths to water between 6 and 10 feet (1.8 to 3 m) were found around the coastline of Long Island Sound at triads 11, 13, 14, 16,and 24. The spatial distribution of the event-based groundwater levels are shown in panel C of Fig. 9. Minimum groundwater depths less than 6 feet (1.8 meters) have the potential to interfere with drainage infrastructure, natural infiltration of soils, and may contribute to more overland runoff during precipitation events (Bosserelle et al., 2022). Groundwater levels between 6 and 15 feet (1.8 to 4.5 m) will likely intersect with basements and other subsurface infrastructure (Conestoga-Rovers and Associates, 2007; New Jersey Department of Environmental Protection, 2021). During most precipitation-surge events, groundwater across the study area was elevated (more shallow) above median levels (Fig. 8). Because of the seasonal pattern of high storm surge, events that were sampled conditioned on surge occurred during the winter when regional groundwater storage and levels are highest (Bjerklie et al., 2012; Li et al., 2015).

Overall compound flood hazard rating was scored according to the criteria described in section 3.4, stratifying the scoring by magnitude of precipitation-surge return period adjustments and shallow (0 to 6 feet or 0 to 1.8 m) versus deeper (6 to 15 feet or 1.8 to 4.6 m) monthly average groundwater levels Fig. 10). Final scores ranged from 1 to 5 and are generally higher (indicating more frequent co-occurrence of high rainfall, surge, and shallow groundwater) on the western south shore of Long Island, as well as along the Connecticut coast. Final compound hazard scores along with their scoring components are shown spatially in Fig. 11, plotted at the centroid of groundwater wells associated with each precipitation–coastal station pair. Interpolated results across the study area are shown in Fig. 11a and as a shapefile in Glas et al. (2025). Compound flood hazard scores were lowest across central and eastern Long Island, both south and north shores. The compound hazard scores, supporting univariate hazard layers, and 900-m gridding geometry are available for interactive exploration at the station-triad and 900-m grid scale via an online mapping application (Finkelstein et al., 2025,

https://ny.water.usgs.gov/maps/compoundflooding/). The individual ordinal components contributing to the composite hazard score shown in Figure 11a are presented in Figures 11b–d: biconditional dependence (11b), upper tail dependence (11c), and shallow groundwater depth (11d).

5 Discussion

The findings from this study demonstrate that there is quantifiable seasonality of compound coastal flood events across the study area (Fig. 4). Storm surges occur more frequently during the winter months when extratropical cyclones are at their strongest (Frame et al., 2017), which is a conclusion consistent with previous studies (e.g., Chen et al., 2024; Liu et al., 2020; Maduwantha et al., 2024) that characterized the temporal variability of coastal storm impacts in this area. For example, Chen et al. (2024) found that tropical storms, which peak in late summer and fall, are associated with the largest compound events around New York City, whereas extratropical cyclones tend to generate more

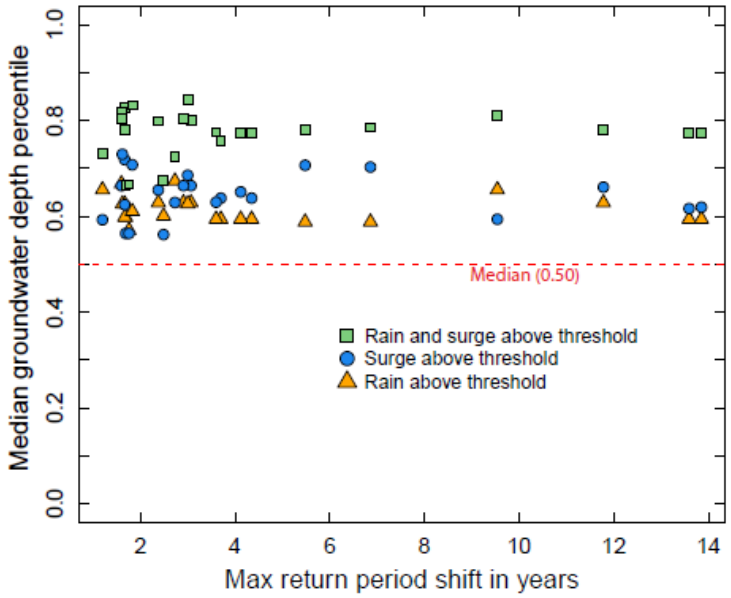

Figure 9. Median groundwater percentiles (based on the full monthly period of record during 1975–2021) during selected events: conditioned on precipitation (CoP), conditioned on surge (CoS), and during all dates where both variables exceeded their respective thresholds. The x-axis represents the maximum return period shift across CoP and CoS for each station triad. The dashed red line indicates the long-term median groundwater level percentile (0.50).

frequent and lower magnitude events. Booth et al. (2016) found that although hurricanes have historically created the conditions for the highest storm surge over the past century along the mid-Atlantic and Northeastern U.S. coastline, moderate storms generated by extratropical cyclones have occurred more frequently, affect larger areas of coastline, and should not be ignored as important drivers of coastal flooding. In addition, the longer durations of extratropical cyclones relative to tropical storms enhance the relative probability that extratropical cyclones will occur during a high tide, whereas compound events generated by shorter duration, more intense tropical systems, may miss the high tides entirely (Marsooli and Wang, 2020).

The results demonstrate spatial variability in precipitation-surge dependence across the study area, with the strongest dependence observed along the south shore of Long Island and interior coastal Connecticut. (Fig. 10a and 10b), which are areas exposed to storm tracks originating both on land and sea (Colle et al., 2010; Liu et al., 2021). Shallow depths to groundwater (Fig. 10c and 11d) and substantial proportions of impervious area attributable to population density make coastal Connecticut and Long Island's south shore vulnerable to damages associated with all three drivers of compound flooding (Bjerklie et al., 2012; Walter et al., 2024). Results from this study show that eastern Long Island, by contrast, showed both the lowest occurrence of compound events and also comprises more natural and agricultural land cover that potentially mitigate flood impacts compared to the more urbanized western part of the island (Glas et al., 2023). The potential for groundwater flooding was considered in this study, though data limitations restricted their direct integration into return period computations. However, the minimum monthly depth to groundwater serves as a valuable precondition for understanding the potential for groundwater flooding during precipitation-surge compound events. Groundwater levels in the uppermost hydrogeologic units throughout the study area are highest (depth to water shallowest) in the winter (Barclay et al., 2024; Walter et al., 2024), when the likelihood of compound events is also highest. Rising sea levels are projected to elevate coastal groundwater tables across the study area, increasing the frequency of shallow groundwater preconditions and likely exacerbating the compound flood hazard documented here (Shepard et al., 2012; Masterson and Garabedian, 2007; Rosenzweig et al., 2024).

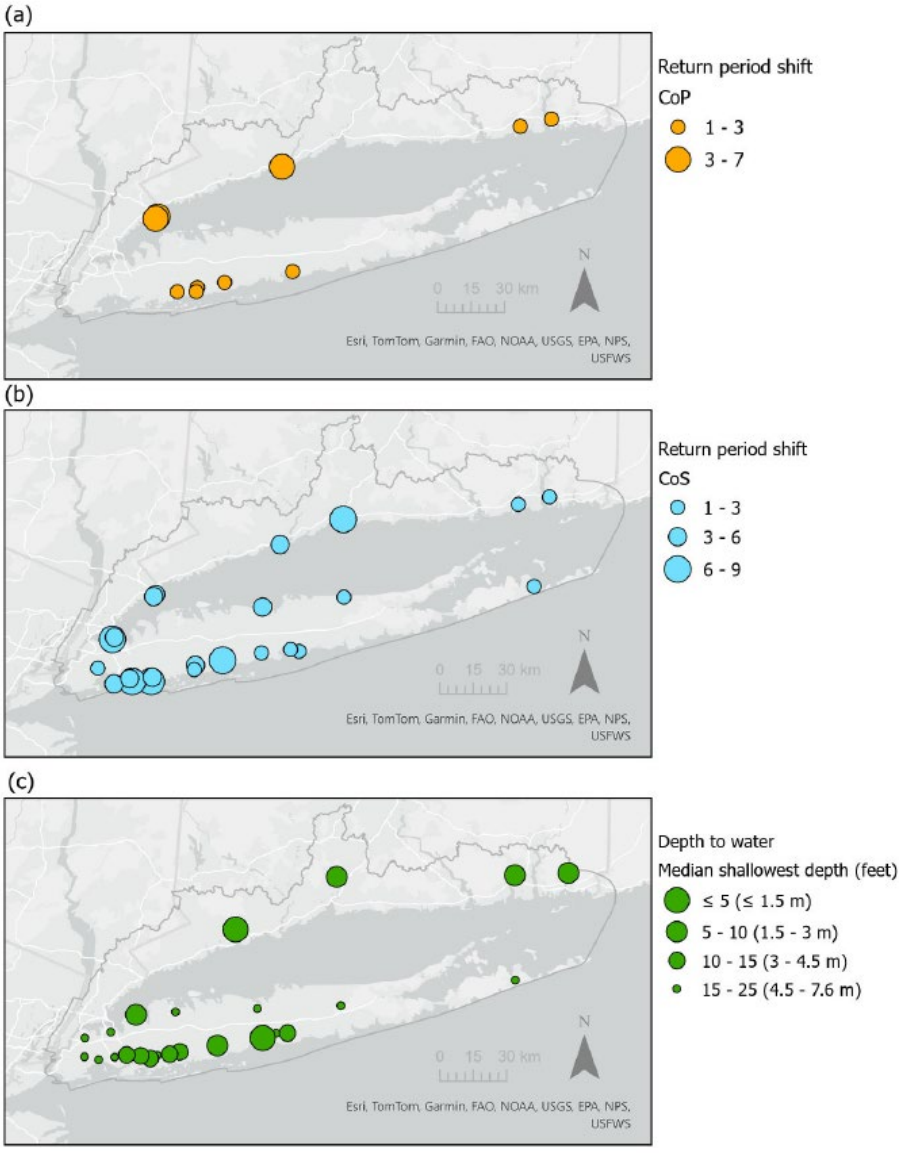

Figure 10. Maps of resulting compound flood hazard. (a) Return period shift for events exceeding threshold values in precipitation-conditioned (CoP) samples. The shift represents the factor difference between assumptions of dependence and independence, averaged using inverse 95% confidence interval weighting across several univariate return periods. (b) Return period shifts conditioned on surge (CoS). (c) Median shallowest groundwater depth (in feet) for well clusters located within the precipitation / surge search radius. The solid grey line delineates the study area boundary. Projection World Geodetic System of 1984, Base modified from U.S. Geological Survey digital data, 1:2,000,000.

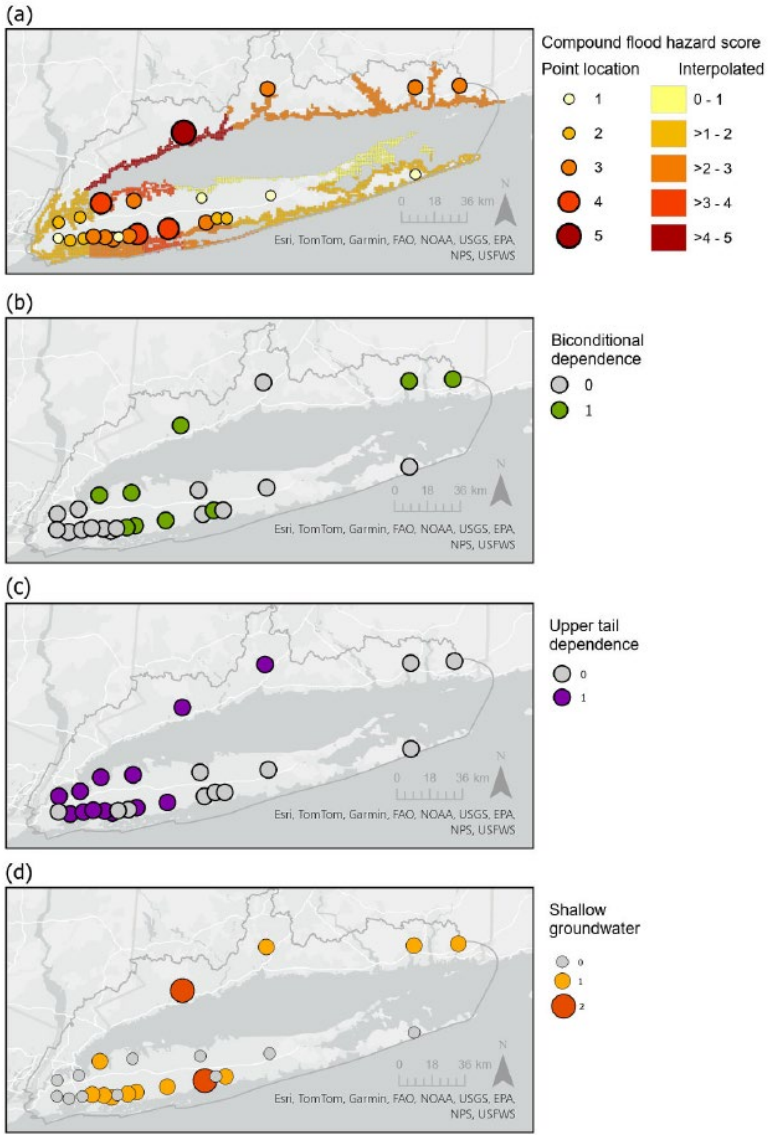

Figure 11. Breakdown of scoring assignments used to compute the compound flood hazard score. (a) Final hazard scores by triad. (b) One point assigned for biconditional dependence, defined as dependence in both rainfall-conditioned (CoP) and surge-conditioned (CoS) samples. (c) One point assigned if either CoP or CoS samples were best fit by a copula model exhibiting upper tail dependence. (d) Groundwater scores based on the median shallowest depth among selected wells per triad: 2 points for less than 6 ft (1.8 m) below land surface (bls), 1 point for 6 to 15 ft (1.8 to 4.6 m) bls, and 0 points for greater than 15 ft (4.6 m) bls. The solid grey line delineates the study area boundary. Boundaries between hazard zones (a) reflect interpolation from 24 discrete station triads and should not be interpreted as precise spatial boundaries. Local variability in precipitation, coastal water levels, and groundwater depth at unsampled locations is not represented.

Record imputation introduces uncertainty into these results, as the quality of gap-filled data directly influences threshold selection, dependence estimation, and groundwater percentile calculations. Extreme values that have been estimated by imputation may be under-represented because of the tendency for regression to underpredict the variance of time series (Newman, 2014), potentially underestimating the true variability and frequency of compound flooding. Imputation techniques that include a maintenance of variance (Vogel and Stedinger, 1985) may yield results that more accurately represent the variance of the system; however, these methods generally have lower predictive power than ordinary least squares or ridge regression (Levy et al., 2025) and should be used with caution if records show autocorrelation patterns typical of coastal water levels and groundwater (Matalas and Jacobs, 1964). To the extent that imputation dampens extreme values, tail dependence estimates and return period adjustments derived from imputed portions of the record may be slightly conservative, representing a lower bound on compound hazard at locations where early NTR and groundwater records relied heavily on imputed values. Formal propagation of imputation uncertainty through the copula framework remains a direction for future work. Data imputation for this study is deemed prudent because imputation gains access to multiple stations throughout the study area that do not have complete data and have been traditionally left out of previous studies of compound flooding in the region (Ghanbari et al., 2021; Lai et al, 2021; Nasr et al., 2023; Wahl et al., 2015).

Threshold selection approaches widely vary across the literature and can introduce variability in the results by influencing sample sizes and consequently the robustness of derived conclusions. Uncertainty associated with different threshold detection and declustering methods can be further increased under potentially nonstationary conditions (Agilan et al., 2021). Employing a variety of threshold selection techniques and investigating the sensitivity of results may be necessary to fully understand the spatial distribution of extreme events. The threshold selection procedure used here, which maximizes Kendall tau within the constraint of 3-6 events per year, may introduce a slight bias toward stronger dependence estimates relative to fixed-threshold approaches. However, the 3-6 events per year constraint limits the range of thresholds available for optimization and therefore the magnitude of any such bias.

Multiple copula models were studied to understand precipitation-surge dependence better, limiting those models to two choices of elliptical copulas and four Archimedean types that may display tail dependence and such tail dependence in the appropriate tail (for this study the upper tail). These choices were based on previous studies (e.g., Phillips et al., 2022) and associated fit metrics for each copula choice. However, some studies have used a single copula model to describe a region so that the differences in dependence arise from the variability of parameter estimates instead of the practitioner's choice of copula model (e.g., Chen et al., 2024). This study incorporates elements of sampling and parameter uncertainty in the bootstrap procedure but does not address imputation uncertainty or model selection uncertainty.

All candidate copula families used in this study are permutation symmetric, meaning $C(u,v) = C(v,u)$, which assumes that the dependence structure is the same regardless of which variable is conditioned upon. Asymmetric copulas, which allow for directional dependence between precipitation and surge, were not considered. If the true dependence structure is asymmetric, the symmetric copulas used here may misrepresent the joint distribution in ways that could affect return period estimates at individual triads. The biconditional sampling approach used in this study, which produces separate CoP and CoS datasets, partially addresses this by allowing dependence to be assessed from both conditioning directions, and differences in results between CoP and CoS provide an indirect indication of potential asymmetry in the data.

Linear regression of POT exceedance magnitudes against time revealed small trends at a subset of triads, with surge extremes showing slight decreasing trends at stations along the western south shore of Long Island and coastal Connecticut (slopes ranging from -0.003 to -0.007 m/year), and no regionally coherent increasing trend in precipitation extremes. These marginal trends are insufficient to justify a nonstationary framework, consistent with the split-period uTDC analysis in Figure 6 and the guidance of Serinaldi and Kilsby (2015).Ultimately, we chose not to implement a nonstationary copula model because changes in tail dependence and overall correlation were judged as not substantial enough over the period of study to merit the introduction of additional uncertainty (Serinaldi and Kilsby, 2015).

6 Conclusion

An analysis of the co-occurrence of high precipitation, storm surge, and shallow groundwater depths was conducted across New York City, Long Island, and southern Connecticut to characterize the spatial distribution of compound flood potential. This study harnessed daily precipitation, storm surge, and monthly groundwater data from multiple stations, employing data imputation techniques to construct a more cohesive regional perspective on compound event occurrences than previous research. We applied bivariate joint probability copula models to estimate the frequency of potentially extreme precipitation-surge events, utilizing a biconditional sampling method that analyses the extremes of each variable alongside the corresponding maximum precipitation or surge values over defined time lags. We quantified the frequency of compound event occurrences through a return period adjustment, representing the ratio of bivariate 'AND' return periods under independence versus dependence assumptions between precipitation and storm surge. A return period adjustment close to one indicates a minimal likelihood of compound events, while larger adjustments signify a substantially increased frequency when dependencies are considered. These adjustments are influenced by the univariate frequencies of interest. To streamline these variations into a single representative value, we calculated a weighted average of shifts, where the weights corresponded to the inverse of model variability derived from bootstrap-style resampling.

Results of this study show a regional gradient of compound flood potential between precipitation and storm surge. Stronger dependence tends to occur along the south shore of Long Island and across interior coastal Connecticut, while smaller adjustments were found for eastern Long Island and New York City. These spatial differences likely reflect regional variability in storm track exposure and coastal morphology, though detailed attribution is beyond the scope of this study. Shallow groundwater conditions amplify this gradient: levels are shallowest in southern Nassau County, where high return period adjustments contribute to hazard scores of 4 out of 5, and in southwestern Connecticut, where the highest hazard scores in the study area (5 out of 5) were observed. These findings underscore the value of integrated compound flood frameworks that consider precipitation, storm surge, and groundwater jointly rather than in isolation, particularly in densely populated coastal zones. Future work should examine process-based interactions during compound events, including

coupled modeling of subsurface infrastructure and drainage, groundwater dynamics, and coastal processes under present and future conditions.

Code and Data Availability

All data and R scripts supporting this study are archived in a U.S. Geological Survey data release (Glas et al., 2025). The release contains input files, both raw and imputed, scripts to replicate the analyses, and associated outputs to ensure full reproducibility.

Author Contributions

RG and LH conceptualized the study approach, with RG leading the analyses, computational code development, and original manuscript preparation. LH conducted the spatial clustering and interpolation of point results to the spatial grid and provided early project management support. SC led the coastal time series data processing and contributed to conceptualization. AH assisted with data processing. KM provided project management support. All co-authors contributed to manuscript review and revision.

Competing Interests

The authors declare that they have no competing interests.

Acknowledgements

This work was supported by the U.S. Environmental Protection Agency Long Island Sound Study and by Hurricane Ida Supplemental appropriations. Any use of trade, firm, or product names is for descriptive purposes only and does not imply endorsement by the U.S. Government. During manuscript revision, Microsoft Copilot (GPT-5-based model) was used to improve grammar, clarity, and coherence of the text. All AI-generated suggestions were reviewed, revised as needed, and approved by the authors to ensure accuracy and maintain the integrity of the scientific content. The authors thank Robert Jane and William Asquith for their thorough internal reviews and constructive feedback, and two anonymous reviewers whose thoughtful comments substantially improved the manuscript.

References

Agel, L., Barlow, M., Qian, J. H., Colby, F., Douglas, E., & Eichler, T. (2015). Climatology of daily precipitation and extreme precipitation events in the northeast United States. Journal of Hydrometeorology, 16(6), 2537-2557. https://doi.org/10.1175/JHM-D-14-0147.1

Agilan, V., Umamahesh, N. V., & Mujumdar, P. P. (2021). Influence of threshold selection in modeling peaks over threshold based nonstationary extreme precipitation series. Journal of Hydrology, 593, 125625. https://doi.org/10.1016/j.jhydrol.2020.125625

Akaike, H. (1973). Maximum likelihood identification of Gaussian autoregressive moving average models. Biometrika, 60(2), 255–265. https://doi.org/10.1093/biomet/60.2.255

Asquith, W.H., Kiang, J.E., and Cohn, T.A., 2017, Application of at-site peak-streamflow frequency analyses for very low annual exceedance probabilities: U.S. Geological Survey Scientific Investigation Report 2017–5038, 93 p., https:// doi.org/10.3133/sir20175038.

Aurenhammer, F. (1991). Voronoi diagrams—a survey of a fundamental geometric data structure. *ACM computing surveys (CSUR)*, *23*(3), 345-405.

Barbot, S., Pineau-Guillou, L., & Delouis, J.-M. (2024). Extreme storm surge events and associated dynamics in the North Atlantic. Journal of Geophysical Research: Oceans, 129, e2023JC020772. https://doi.org/10.1029/2023JC020772

Barclay, J.R., Holland, M.J., and Mullaney, J.R., 2024, Simulated mean monthly groundwater-transported nitrogen loads in watersheds on the north shore of Long Island Sound, 1993–2022: U.S. Geological Survey Scientific Investigations Report 2024–5090, 63 p., https://doi.org/10.3133/sir20245090

Bjerklie, D.M., Mullaney, J.R., Stone, J.R., Skinner, B.J., and Ramlow, M.A., 2012, Preliminary investigation of the effects of sea-level rise on groundwater levels in New Haven, Connecticut: U.S. Geological Survey Open-File Report 2012–1025, 46 p., https://doi.org/10.3133/ofr20121025

Booth, J. F., Rieder, H. E., & Kushnir, Y. (2016). Comparing hurricane and extratropical storm surge for the Mid-Atlantic and Northeast Coast of the United States for 1979–2013. Environmental Research Letters, 11(9), 094004. **DOI** 10.1088/1748-9326/11/9/094004

Bosserelle, A. L., Morgan, L. K., & Hughes, M. W. (2022). Groundwater rise and associated flooding in coastal settlements due to sea-level rise: a review of processes and methods. Earth's Future, 10(7), **https://doi.org/10.1029/2021EF002580**

Brunner, M. I., Seibert, J., & Favre, A. C. (2016). Bivariate return periods and their importance for flood peak and volume estimation. Wiley Interdisciplinary Reviews: Water, 3(6), 819–833, **https://doi.org/10.1002/wat2.1173**

Chen, Z., Orton, P., Booth, J., Wahl, T., DeGaetano, A., Kaatz, J., & Horton, R. (2024). Influence of storm type on compound flood hazard of a mid-latitude coastal-urban environment. Hydrology and Earth System Sciences Discussions, 2024, 1–30. https://doi.org/10.5194/hess-2024-135

Coch, N. K. (2015). Unique vulnerability of the New York–New Jersey metropolitan area to hurricane destruction. Journal of Coastal Research, 31(1), 196–212. **https://doi.org/10.2112/JCOASTRES-D-13-00183.1**

Colle, B. A., Rojowsky, K., & Buonaito, F. (2010). New York City storm surges: Climatology and an analysis of the wind and cyclone evolution. Journal of Applied Meteorology and Climatology, 49(1), 85–100. https://doi.org/10.1175/2009JAMC2189.1

Conestoga-Rovers and Associates, 2007. Revised Work Plan Vapor Intrusion Pathway Assessment, Bruno Cooperative Association, Associated Properties Superfund Site, Bruno, Nebraska, Consent Decree No. 8:02CV483. Accessed August 15, 2024 at https://semspub.epa.gov/work/07/30222021.pdf

Cook, S.E. and Herdman, L.M., 2025, Geospatial dataset of coastal-inundation maps for Long Island and Long Island Sound (CT/NY): U.S. Geological Survey data release, https://doi.org/10.5066/P94P4WXX.

DeGaetano, A. T. (2008). Predictability of seasonal east coast winter storm surge impacts with application to New York's Long Island. Meteorological Applications, 15(2), 231–242. **https://doi.org/10.1002/met.59**

Fallon, K., & Kuonen, J. (2023). Understanding Perceptions and Needs around Flooding and Erosion Risk for Shoreline Communities in Long Island and the Hudson River Estuary, New York. https://doi.org/10.25923/64hy-g695

Favre, A. C., El Adlouni, S., Perreault, L., Thiémonge, N., & Bobée, B. (2004). Multivariate hydrological frequency analysis using copulas. Water Resources Research, 40(1). **https://doi.org/10.1029/2003WR002456**

Finkelstein, J.S., Herdman, L.M., Masterson, K.K., Glas, R.L., Cook, S.E., and Welk, R.J., 2025, Compound Flooding Hazard Assessment: U.S. Geological Survey Web Map, https://ny.water.usgs.gov/maps/compoundflooding/

Forman, A. (2014). Caution Ahead: Overdue Investments for New York's Aging Infrastructure. Center for an Urban Future. https://eric.ed.gov/?id=ED555648

Frame, T., Harrison, G., Hewson, T., & Roberts, N. (2017). Meteorological risk: Extra-tropical cyclones, tropical cyclones and convective storms. In K. Poljanšek, M. Marin Ferrer, T. De Groeve, & I. Clark (Eds.), Science for disaster risk management 2017: Knowing better and losing less (pp. 246–256). Publications Office of the European Union. https://doi.org/10.2760/17520

Genest, C. and A. C. Favre (2007). Everything you always wanted to know about copula modeling but were afraid to ask. Journal of Hydrologic Engineering, 12 (4), 347–368. https://doi.org/10.1061/(ASCE)1084-0699(2007)12:4(347)

Ghanbari, M., Arabi, M., Kao, S. C., Obeysekera, J., & Sweet, W. (2021). Climate change and changes in compound coastal-riverine flooding hazard along the US coasts. Earth's Future, 9(5), e2021EF002055. **https://doi.org/10.1029/2021EF002055**

Glas, R., Hecht, J., Simonson, A., Gazoorian, C., & Schubert, C. (2023). Adjusting design floods for urbanization across groundwater-dominated watersheds of Long Island, NY. Journal of Hydrology, 618, 129194. https://doi.org/10.1016/j.jhydrol.2023.129194

Glas, R., Herdman, L., Cook, S., Masterson, K., 2025, Supporting Datasets and R Code for Compound Flood Hazard Modeling in the New York - Long Island Sound Region. U.S. Geological Survey data release, https://doi.org/10.5066/P13ARD2K.

Green, J., Haigh, I. D., Quinn, N., Neal, J., Wahl, T., Wood, M., Eilander, D., de Ruiter, M., Ward, P., and Camus, P., (2024). A comprehensive review of coastal compound flooding literature. arXiv preprint arXiv:2404.01321.https://doi.org/10.48550/arXiv.2404.01321

Hanchey A, Schnall A, Bayleyegn T, et al. *Notes from the Field:* Deaths Related to Hurricane Ida Reported by Media — Nine States, August 29–September 9, 2021. MMWR Morb Mortal Wkly Rep 2021;70:1385–1386. DOI: http://dx.doi.org/10.15585/mmwr.mm7039a3

Herreros-Cantis, P., Olivotto, V., Grabowski, Z. J., & McPhearson, T. (2020). Shifting landscapes of coastal flood risk: Environmental (in) justice of urban change, sea level rise, and differential vulnerability in New York City. Urban Transformations, 2(1), 9, https://doi.org/10.1186/s42854-020-00014-w

Huang, W., & Prokhorov, A. (2014). A goodness-of-fit test for copulas. Econometric Reviews, 33(7), 751–771. https://doi.org/10.1080/07474938.2012.690692

Jane, R., Cadavid, L., Obeysekera, J., and Wahl, T. (2020). Multivariate statistical modelling of the drivers of compound flood events in South Florida, Nat. Hazards Earth Syst. Sci., 20, 2681–2699, https://doi.org/10.5194/nhess-20-2681-2020.

Jane, R.A., Malagón-Santos, V., Rashid, M.M., Doebele, L., Wahl, T., Timmers, S.R., Serafin, K.A., Schmied, L. and Lindemer, C., 2022. A hybrid framework for rapidly locating transition zones: A comparison of event-and response-based return water levels in the Suwannee River FL. Water Resources Research, 58(11), p.e2022WR032481. **https://doi.org/10.1029/2022WR032481**

Kouhi, S., Hashemi, M. R., Spaulding, M., & Hara, T. (2022). Modeling the impact of sea level rise on maximum water elevation during storm surge events: a closer look at coastal embayments. Climatic Change, 171(3), 31. https://doi.org/10.1007/s10584-022-03342-x

Kunkel, K. E., Karl, T. R., Squires, M. F., Yin, X., Stegall, S. T., & Easterling, D. R. (2020). Precipitation extremes: Trends and relationships with average precipitation and precipitable water in the contiguous United States. Journal of Applied Meteorology and Climatology, 59(1), 125–142. https://doi.org/10.1175/JAMC-D-19-0185.1

Lai, Y., Li, J., Gu, X., Liu, C., & Chen, Y. D. (2021). Global compound floods from precipitation and storm surge: Hazards and the roles of cyclones. Journal of Climate, 34(20), 8319–8339. https://doi.org/10.1175/JCLI-D-21-0050.1

Liu, C., Onat, Y., Jia, Y., & O'Donnell, J. (2021). Modeling nearshore dynamics of extreme storms in complex environments of Connecticut. *Coastal Engineering*, *168*, 103950. https://doi.org/10.1016/j.coastaleng.2021.103950

Levy, Z. F., Glas, R. L., Stagnitta, T. J., & Terry, N. (2025). ARCHI: A New R Package for Automated Imputation of Regionally Correlated Hydrologic Records. Groundwater. https://doi.org/10.1111/gwat.13474

Levy, Z. F., Stagnitta, T. J., and Glas, R. L., 2024, ARCHI: Automated Regional Correlation Analysis for Hydrologic Record Imputation, v1.0.0: U.S. Geological Survey software release, https://doi.org/10.5066/P1VVHWKE.

Li, B., Rodell, M., & Famiglietti, J. S. (2015). Groundwater variability across temporal and spatial scales in the central and northeastern US. Journal of Hydrology, 525, 769–780. https://doi.org/10.1016/j.jhydrol.2015.04.033

Liu, C., Jia, Y., Onat, Y., Cifuentes-Lorenzen, A., Ilia, A., McCardell, G., Fake, T., & O'Donnell, J. (2020). Estimating the Annual Exceedance Probability of Water Levels and Wave Heights from High Resolution Coupled Wave-Circulation Models in Long Island Sound. *Journal of Marine Science and Engineering*, *8*(7), 475. https://doi.org/10.3390/jmse8070475

Maduwantha, P., Wahl, T., Santamaria-Aguilar, S., Jane, R., Booth, J. F., Kim, H., and Villarini, G.: A multivariate statistical framework for mixed storm types in compound flood analysis, Nat. Hazards Earth Syst. Sci., 24, 4091–4107, https://doi.org/10.5194/nhess-24-4091-2024, 2024.

Marsooli R and Wang Y (2020) Quantifying tidal phase effects on coastal flooding induced by Hurricane Sandy in Manhattan, New York using a micro-scale hydrodynamic model. Front. Built Environ. 6:149. doi: 10.3389/fbuil.2020.00149

Masterson, J. P., & Garabedian, S. P. (2007). Effects of sea-level rise on ground water flow in a coastal aquifer system. *Groundwater*, *45*(2), 209-217.

Masterson, K.K., Welk, R.J., Barclay, J.R., Jahn, K.L., and Herdman, L.M., 2025, A spatial analysis of the groundwater emergence flood hazard in Long Island, New York and near coastal areas surrounding Long Island Sound in New York, Connecticut, and Rhode Island: EarthArXiv preprint, https://doi.org/10.31223/X5HB28.

Matalas, N.C., and Jacobs, B.A., (1964), A correlation procedure for augmenting hydrologic data. U.S. Geological Survey Professional Paper 434-E, 7p. https://doi.org/10.3133/pp434E

MacQueen, J.: Some methods for classification and analysis of multivariate observations, in: Proceedings of the Fifth Berkeley Symposium on Mathematical Statistics and Probability, Volume 1: Statistics, edited by: Cam, L. M. L. and Neyman, J., University of California Press, 281–297, 1967.

Nagler, T., Schepsmeier, U., Stoeber, J., Brechmann, E.C., Graeler, B., Erhardt, T., Almeida, C., Min, A., Czado, C., Hofmann, M., Killiches, M., Joe, H., & Vatter, T. (2023), VineCopula: statistical inference of vine copulas, https://doi.org/10.32614/CRAN.package.VineCopula version 2.5.0, dated July 10, 2023

Nasr, A. A., Wahl, T., Rashid, M. M., Jane, R. A., Camus, P., & Haigh, I. D. (2023). Temporal changes in dependence between compound coastal and inland flooding drivers around the contiguous United States coastline. Weather and Climate Extremes, 41, 100594. https://doi.org/10.1016/j.wace.2023.100594

Nederhoff, K., Leijnse, T. W., Parker, K., Thomas, J., O'Neill, A., van Ormondt, M., McCall, R., Erikson, L., Barnard, P.L., Foxgrover, A., & Klessens, W. (2024). Tropical or extratropical cyclones: what drives the compound flood hazard, impact, and risk for the United States Southeast Atlantic coast?. Natural Hazards, pp.1–47. https://doi.org/10.1007/s11069-024-06552-x

New Jersey Department of Environmental Protection, 2021. Vapor Intrusion Technical Guidance Version5.0. Accessed August 15, 2024 at https://dep.nj.gov/srp/guidance/vapor-intrusion/

Newman, D. A. (2014). Missing data: Five practical guidelines. Organizational research methods, 17(4), 372–411. https://doi.org/10.1177/1094428114548590

NOAA Center for Operational Oceanographic Products and Services (CO-OPS). (2023). *Tides & Currents: Water Level Observations* [Data set]. National Oceanic and Atmospheric Administration, U.S. Department of Commerce. Retrieved October 1, 2023, from https://tidesandcurrents.noaa.gov

NOAA National Centers for Environmental Information (NCEI). (2023). *Daily Summaries: Global Historical Climatology Network (GHCN-Daily)* [Data set]. U.S. Department of Commerce. Retrieved October 1, 2023, from https://www.ncei.noaa.gov

O'Donnell, J., & O'Donnell, J. E. (2012). Coastal vulnerability in Long Island Sound: The spatial structure of extreme sea level statistics. In 2012 Oceans (pp. 1–4). IEEE. 10.1109/OCEANS.2012.6405099

Orton, P., Georgas, N., Blumberg, A., & Pullen, J. (2012). Detailed modeling of recent severe storm tides in estuaries of the New York City region. Journal of Geophysical Research: Oceans, 117(C9). **https://doi.org/10.1029/2012JC008220**

Pedregosa, F., Varoquaux, G., Gramfort, A., Michel, V., Thirion, B., Grisel, O., Blondel, M., Prettenhofer, P., Weiss, R., Dubourg, V., Vanderplas, J., Passos, A., Cournapeau, D., Brucher, M., Perrot, M., and Duchesnay, É.: Scikit-learn: Machine Learning in Python, J. Mach. Learn. Res., 12, 2825–2830, 2011.

Phillips, R. C., Samadi, S., Hitchcock, D. B., Meadows, M. E., & Wilson, C. A. M. E. (2022). The devil is in the tail dependence: An assessment of multivariate copula-based frameworks and dependence concepts for coastal compound flood dynamics. Earth's Future, 10(9), e2022EF002705. **https://doi.org/10.1029/2022EF002705**

R Core Team. (2024). *R: A language and environment for statistical computing*. R Foundation for Statistical Computing, Vienna, Austria. https://www.R-project.org/

Rosenzweig, B., Montalto, F. A., Orton, P., Kaatz, J., Maher, N., Kleyman, J. et al. (2024). NPCC4: Climate Change and New York City's Flood Risk. Annals of the New York Academy of Sciences, 1539, 127-184.https://doi.org/10.1111/nyas.15175

Salvadori, G. (2004). Bivariate return periods via 2-copulas. Statistical Methodology, 1(1-2), 129–144. https://doi.org/10.1016/j.stamet.2004.07.002

Salvadori, G., & De Michele, C. (2007). On the use of copulas in hydrology: Theory and practice. Journal of Hydrologic Engineering, 12(4), 369–380. https://doi.org/10.1061/(ASCE)1084-0699(2007)12:4(369

Salvadori, G., & De Michele, C. (2010). Multivariate multiparameter extreme value models and return periods: A copula approach. Water Resources Research, 46(10). **https://doi.org/10.1029/2009WR009040**

Serinaldi, F., & Kilsby, C. G. (2015). Stationarity is undead: Uncertainty dominates the distribution of extremes. Advances in Water Resources, 77, 17–36. https://doi.org/10.1016/j.advwatres.2014.12.013

Shepard, C. C., Agostini, V. N., Gilmer, B., Allen, T., Stone, J., Brooks, W., & Beck, M. W. (2012). Assessing future risk: quantifying the effects of sea level rise on storm surge risk for the southern shores of Long Island, New York. Natural Hazards, 60, 727–745. https://doi.org/10.1007/s11069-011-0046-8

Shiau, J. T. (2003). Return period of bivariate distributed extreme hydrological events. Stochastic Environmental Research and Risk Assessment, 17, 42–57. https://doi.org/10.1007/s00477-003-0125-9

Strauss, B. H., Orton, P. M., Bittermann, K., Buchanan, M. K., Gilford, D. M., Kopp, R. E., Kulp, S., Massey, C., de Moel, H., & Vinogradov, S. (2021). Economic damages from Hurricane Sandy attributable to sea level rise caused by anthropogenic climate change. Nature Communications, 12, 2720. https://doi.org/10.1038/s41467-021-22838-1

Su, X., Belvedere, P., Tosco, T., & Prigiobbe, V. (2022). Studying the effect of sea level rise on nuisance flooding due to groundwater in a coastal urban area with aging infrastructure. Urban Climate, 43, 101164. https://doi.org/10.1016/j.uclim.2022.101164

Suffolk County DMA 2000 Hazard Mitigation Plan Update – Suffolk County, New York, section 5.4.15: shallow groundwater flooding, 2020.

https://www.southamptontownny.gov/DocumentCenter/View/24204/Section-5415---Shallow-GW-Flooding

U.S. Geological Survey, 2023, USGS water data for the Nation: U.S. Geological Survey National Water Information System database, accessed June 8, 2023, at https://doi.org/10.5066/F7P55KJN.

U.S. Geological Survey, 2025, Long Island Sound compound flooding mapper: U.S. Geological Survey web page, accessed [April 10 2026], at https://ny.water.usgs.gov/maps/compoundflooding/

U.S. Census Bureau. (2023). *County Population Totals: 2020–2024*. Table CO-EST2023-POP, U.S. Department of Commerce. Retrieved [11 1, 2023], from: https://www.census.gov/data/tables/time-series/demo/popest/2020s-counties-total.html

Vogel, R. M., & Stedinger, J. R. (1985). Minimum variance streamflow record augmentation procedures. Water Resources Research, 21(5), 715–723. **https://doi.org/10.1029/WR021i005p00715**

Wahl, T., Jain, S., Bender, J., Meyers, S. D., & Luther, M. E. (2015). Increasing risk of compound flooding from storm surge and precipitation for major US cities. Nature Climate Change, 5(12), 1093–1097. https://doi.org/10.1038/nclimate2736

Walter, D.A., Jahn, K.L., Masterson, J.P., Dressler, S.E., Finkelstein, J.S., and Monti, J., Jr., 2024, Simulation of groundwater flow in the Long Island, New York regional aquifer system for pumping and recharge conditions from 1900 to 2019: U.S. Geological Survey Scientific Investigations Report 2024–5044, 113 p., https://doi.org/10.3133/sir20245044.

Welk, R.J., Masterson, K.K, Barclay, J.R., and Jahn, K.L., 2025a, Geospatial datasets of factors influencing groundwater emergence flood hazard in Long Island, New York and near coastal areas surrounding Long Island Sound in New York, Connecticut, and Rhode Island: U.S. Geological Survey data release, https://doi.org/10.5066/P9W4QIV5.

Welk, R.J., Fisher, B.N., Glas, R.L., Herdman, L.M., Jahn, K.L., Masterson, K.K., 2025b, Geospatial datasets of factors influencing pluvial flood potential in Long Island, New York and near

coastal areas surrounding Long Island Sound in New York, Connecticut, and Rhode Island. U.S. Geological Survey data release, https://doi.org/10.5066/10.5066/P9N6J1SN.

Wong, K. C. (1990). Sea level variability in Long Island Sound. Estuaries, 13, 362–372. https://doi.org/10.2307/1351781

Zscheischler, J., & Seneviratne, S. I. (2017). Dependence of drivers affects risks associated with compound events. *Science advances*, *3*(6), DOI: 10.1126/sciadv.1700263

Triad	Station ID_{pcpt}	$Long_{pcpt}$	Lat_{pcpt}	Station $ID_{coastal}$	$Agency_{coastal}$	$Long_{coastal}$	$Lat_{coastal}$	$Gw_{rad, km}$	Gw_{nwells}	$Long_{GW}$	Lat_{GW}	Map ID
1	USW00094789	-73.7639	40.6392	01311875	USGS	-73.885136	40.57371636	8	3	40.66038142	-73.85207963	R1- C1
2	USW00094789	-73.7639	40.6392	01311850	USGS	-73.7579103	40.6173266	6	2	40.67038128	-73.7869389	R1- C2
3	USW00014732	-73.8803	40.7794	8516945	NOAA	-73.7650033	40.80999678	5	3	40.77248147	-73.80349073	R2- C3
4	USW00014732	-73.8803	40.7794	8516990	NOAA	-73.78166929	40.79333757	9	2	40.74863888	-73.90804169	R2- C4
5	USW00094789	-73.7639	40.6392	01310521	USGS	-73.5754058	40.6276026	5	2	40.66530555	-73.64354169	R1- C5
6	USW00094789	-73.7639	40.6392	01310740	USGS	-73.5837396	40.5934366	8	3	40.67594172	-73.68191403	R1- C6
7	USW00094789	-73.7639	40.6392	01311145	USGS	-73.7373543	40.59316026	9	4	40.67966767	-73.7386687	R1- C7
8	USW00054787	-73.4164	40.7344	01310521	USGS	-73.5754058	40.6276026	6	2	40.69148991	-73.52373709	R3- C5
9	USW00054787	-73.4164	40.7344	01310740	USGS	-73.5837396	40.5934366	13	2	40.68242593	-73.56518865	R3- C6
10	USW00054787	-73.4164	40.7344	01311145	USGS	-73.7373543	40.59316026	6	6	40.67746142	-73.61586381	R3- C7
11	USC00067970	-73.5475	41.1247	8516945	NOAA	-73.7650033	40.80999678	15	4	40.84183701	-73.70124159	R4- C3
12	USC00067970	-73.5475	41.1247	8516990	NOAA	-73.78166929	40.79333757	22	3	40.85384259	-73.54185187	R4- C4
13	USC00063207	-72.0378	41.3503	01194796	USGS	-72.3459166	41.3125983	18	2	41.40519723	-72.17144725	R5- C8
14	USC00063207	-72.0378	41.3503	8461490	NOAA	-72.09499657	41.37167072	23	2	41.41445834	-71.95556669	R5- C9
15	USW00094789	-73.7639	40.6392	8518750	NOAA	-74.0150011	40.70000404	5	8	40.67155779	-73.90988824	R1- C10
16	USW00054787	-73.4164	40.7344	01309225	USGS	-73.3556765	40.66926687	5	4	40.717625	-73.37287499	R3- C11
17	USW00004781	-73.1019	40.7939	01309225	USGS	-73.3556765	40.66926687	5	2	40.74805554	-73.1894861	R6- C11
18	USW00054790	-72.8675	40.8211	01309225	USGS	-73.3556765	40.66926687	5	2	40.76749999	-73.1363472	R7- C11
19	US1NYSF0123	-72.7981	40.8068	01309225	USGS	-73.3556765	40.66926687	8	3	40.76776851	-73.08955553	R8- C11
20	USC00300889	-72.2978	40.9519	8510560	NOAA	-71.95930163	41.04812618	5	3	40.98185951	-72.17026343	R9- C12
21	USC00301309	-73.3731	40.8833	8514560	NOAA	-73.07666422	40.95000233	8	2	40.86670833	-73.21156945	R10- C13
22	USC00307134	-72.7161	40.9625	8514560	NOAA	-73.07666422	40.95000233	12	2	40.879	-72.87479165	R11- C13
23	USW00094702	-73.1267	41.1642	8467150	NOAA	-73.18166364	41.1733364	13	4	41.18623542	-73.2990625	R12- C14
24	USW00014758	-72.8892	41.2589	8465705	NOAA	-72.9083334	41.28333752	15	3	41.39843517	-72.89087036	R13- C15

Table 1. Station triad locations and associated precipitation (pcpt) and coastal station identification numbers (Station ID), including Map IDs referenced in Fig. 1. Agency operating each coastal station indicated as either U.S. Geological Survey (USGS) or National Oceanic and Atmospheric Administration (NOAA) indicated as $Agency_{coastal}$. Each triad consists of a National Oceanic and Atmospheric Administration (NOAA) precipitation gage (NOAA NCEI, 2023), a U.S. Geological Survey (2023) or NOAA tidal station (NOAA CO-OPS, 2023), and the centroid of a number of clustered groundwater observation wells (GWnwells, U.S. Geological Survey, 2023) selected within the search radius in kilometers (GWrad,km) centered on the precipitation–tidal station midpoint.

	RMSE	Average Bias
PPT_{wet}	8.96 mm	-1.49 mm
$PPT*_{dry}$	1.66 mm	0.34 mm
$PPT*_{all}$	4.59 mm	-0.08 mm
NTR	0.09 m	-0.0011 m
GW	1.1 ft (0.34 m)	-0.0012 ft (-0.00037 m)

*ARCHI imputed values have been censored such that values less than 1mm are forced to zero.

Table 2. Imputation performance statistics from a 5% holdout analysis conducted separately for wet days (precipitation (PPT) > 1 mm) and dry days (precipitation = 0 mm). Metrics include root mean square error (RMSE) and average bias between withheld and imputed values, reported in the original units of each variable (millimeters for precipitation, meters for NTR, and feet for groundwater).

Triad	Thr_{pcpt}	N_{CoP}	Tau_{CoP}	$Pcorr_{CoP}$	EPY_{pcpt}	Thr_{SG}	N_{CoS}	Tau_{CoS}	$Pcorr_{CoS}$	EPY_{SG}
1	0.99	167	0.069	0.19	3.21	0.98	201	0.12	**0.012**	3.87
2	0.99	167	0.08	0.12	3.21	0.98	201	0.13	**0.0062**	3.87
3	0.99	169	0.077	0.14	3.25	0.98	202	0.12	**0.009**	3.88
4	0.99	169	0.069	0.19	3.25	0.97	265	0.16	**0.00017**	5.1
5	0.99	167	0.065	0.21	3.21	0.98	198	0.12	**0.01**	3.81
6	0.99	167	0.066	0.21	3.21	0.97	272	0.12	**0.0033**	5.23
7	0.99	167	0.069	0.19	3.21	0.97	268	0.11	**0.01**	5.15
8	0.98	296	0.092	**0.018**	5.69	0.98	198	0.11	**0.019**	3.81
9	0.98	296	0.088	**0.025**	5.69	0.98	199	0.11	**0.017**	3.83
10	0.98	296	0.083	**0.033**	5.69	0.98	200	0.09	0.058	3.85
11	0.98	298	0.092	**0.018**	5.73	0.98	202	0.11	**0.023**	3.88
12	0.98	298	0.087	**0.025**	5.73	0.97	265	0.18	**1.30E-05**	5.1
13	0.98	305	0.081	**0.034**	5.87	0.97	271	0.16	**7.60E-05**	5.21
14	0.98	305	0.077	**0.045**	5.87	0.97	286	0.14	**0.00034**	5.5
15	0.99	167	0.077	0.14	3.21	0.98	201	0.13	**0.0046**	3.87
16	0.98	296	0.094	**0.016**	5.69	0.97	268	0.14	**0.00092**	5.15
17	0.99	170	-0.019	0.72	3.27	0.97	268	0.11	**0.0052**	5.15
18	0.98	296	0.092	**0.018**	5.69	0.97	268	0.16	**9.90E-05**	5.15
19	0.98	297	-0.041	0.29	5.71	0.97	268	0.17	**4.10E-05**	5.15
20	0.98	301	-0.052	0.18	5.79	0.97	272	0.098	**0.016**	5.23
21	0.98	298	0.019	0.62	5.73	0.97	271	0.17	**2.80E-05**	5.21
22	0.98	308	0.051	0.19	5.92	0.97	271	0.19	**3.60E-06**	5.21
23	0.99	162	0.11	**0.04**	3.12	0.98	202	0.14	**0.0043**	3.88
24	0.99	164	0.05	0.35	3.15	0.97	270	0.12	**0.0032**	5.19

Table 3. Summary of biconditional samples for rainfall and coastal storm surge. The table includes selected threshold quantiles (Thr), Kendall's tau correlation coefficients (Tau) and corresponding p-values (Pcorr), and the average number of events per year (EPY). Values are shown for precipitation (pcpt), surge (SG), and the number (N) of bivariate events conditioned on precipitation (CoP) and conditioned on surge (CoS). Bold P values indicate tau is significant.

	Conditioned on Rain					Conditioned on Surge				
Triad	Copula family	Parameter estimate	P_{GOF}	ΔAIC	ΔuTDC	Copula family	Parameter estimate	P_{GOF}	ΔAIC	ΔuTDC
1	Independence	-	-	-	-	Gumbel	1.1	0.22	0	0.082
2	Independence	-	-	-	-	Survival Clayton	0.27	0.96	0	0.067
3	Independence	-	-	-	-	Survival Clayton	0.29	0.52	0	0
4	Independence	-	-	-	-	Survival Clayton	0.35	0.5	0.37	0.085
5	Independence	-	-	-	-	Survival Clayton	0.27	0.8	0	0.056
6	Independence	-	-	-	-	Gumbel	1.1	0.98	0	0.028
7	Independence	-	-	-	-	Gumbel	1.1	0.72	0	0.056
8	Gaussian	0.16	0.51	0	0.083	Survival Clayton	0.23	0.39	0	0.049
9	Gaussian	0.16	0.63	0	0.083	Frank	1	0.64	0.27	0
10	Gaussian	0.15	0.65	0	0.083	Independence	-	-	-	-
11	Gumbel	1.1	0.55	0	0.056	Gumbel	1.1	0.73	0	0.046
12	Survival Clayton	0.19	0.56	0	0	Gaussian	0.29	0.29	0	0.11
13	Frank	0.72	0.76	0	0.062	Frank	1.5	0.67	1.3	0.077
14	Frank	0.68	0.4	0	0.062	Frank	1.3	0.18	0	0.071
15	Independence	-	-	-	-	Gaussian	0.23	0.12	0	0
16	Gaussian	0.17	0.9	0	0.083	Gumbel	1.1	0.32	0	0.082
17	Independence	-	-	-	-	Frank	1.1	0.91	0	0.082
18	Frank	0.83	0.33	0	0.067	Frank	1.5	0.41	0	0
19	Independence	-	-	-	-	Frank	1.6	0.15	0	0
20	Independence	-	-	-	-	Frank	0.89	0.65	0	0.009
21	Independence	-	-	-	-	Gaussian	0.26	0.9	0	0.043
22	Independence	-	-	-	-	Frank	1.7	0.53	0	0.006
23	Survival Clayton	0.21	0.57	0.58	0	Gumbel	1.2	0.15	0	0
24	Independence	-	-	-	-	Gumbel	1.1	0.23	0	0.09

Table 4. Selected copula models and their corresponding parameter estimates, along with ΔAIC and ΔuTDC values used in the model selection process. ΔuTDC represents the difference between the empirical upper tail dependence coefficient and the median of the bootstrapped fitted model estimates. P values are presented for the semi-parametric goodness of fit test ($P_{GOF,}$ Huang and Prokhorov, 2014). Dashes indicate that independence copula was fit and no parameters are applicable.

Triad	$RPshift_{CoP}$	$RPshift_{CoS}$	GW	GW score	Biconditional Dependence Score	Upper Tail Dependence Score	Component Score Sum	Final Hazard Score
1		5.62	15.77	0	0	1	1	2
2		5.47	15.84	0	0	1	1	2
3		5.84	21.1	0	0	1	1	2
4		8.51	15.86	0	0	1	1	2
5		5.33	14.26	1	0	1	2	3
6		7.43	13.83	1	0	1	2	3
7		7	11.91	1	0	1	2	3
8	2.45	4.67	14.19	1	1	1	3	4
9	2.38	1.55	11.44	1	1	0	2	3
10	2.33		16.42	0	0	0	0	1
11	6.86	5	8.65	1	1	1	3	4
12	5.48	3.82	19.03	0	1	1	2	3
13	1.37	1.86	8.76	1	1	0	2	3
14	1.37	1.76	8.91	1	1	0	2	3
15		2.76	16.26	0	0	0	0	1
16	2.48	7.38	8.26	1	1	1	3	4
17		1.57	0	2	0	0	2	3
18	1.45	1.85	20.01	0	1	0	1	2
19		1.92	14.96	1	0	0	1	2
20		1.47	19.14	0	0	0	0	1
21		3.56	20.67	0	0	0	0	1
22		2.01	24.83	0	0	0	0	1
23	3.74	5.94	2.19	2	1	1	4	5
24		7.05	9.64	1	0	1	2	3

Table 5. Summary of average return period shifts for rain–surge events conditioned on precipitation (CoP) and on surge (CoS), along with the shallowest depth to groundwater (GW, in feet) for each well cluster associated with a triad during independent precipitation-surge co-occurrences. Component-based scores for groundwater depth, biconditional dependence, and upper tail dependence were summed and scaled to produce an integrated composite hazard rating (Final Hazard Score). Data available in Glas et al. (2025).